

## Snow scattering signals in ground-based passive microwave radiometer measurements

Stefan Kneifel,<sup>1</sup> U. Löhnert,<sup>1</sup> A. Battaglia,<sup>2</sup> S. Crewell,<sup>1</sup> and D. Siebler<sup>3</sup>

Received 11 January 2010; revised 7 April 2010; accepted 28 April 2010; published 31 August 2010.

[1] This paper investigates the influence of snow microphysical parameters on the enhancement of ground-based passive microwave brightness temperature (TB) measurements. In addition to multispectral passive microwave observations between 20 and 150 GHz, a 35 GHz cloud radar and a 2-D video disdrometer for in situ measurements of snowfall were deployed as part of the “towards an optimal estimation-based snowfall characterization algorithm” campaign in the winter season of 2008–2009 at an Alpine environment located at 2650 m mean sea level. These observations are combined with nearby radiosonde ascents and surface standard meteorological measurements to reconstruct the atmospheric state (i.e., fields of temperature, humidity, snow, and liquid water contents) and are subsequently used as input for a microwave radiative transfer (RT) model. We investigate the sensitivity of the missing information about snow shape and snow particle size distribution (SSD) on the microwave TB measurements using the disdrometer data as a rough constraint. For an extended case study, we found that TBs at 90 and 150 GHz are significantly enhanced because of scattering of surface radiation at snow crystals and that this enhancement is clearly correlated with the radar derived snow water path ( $SWP < 0.2 \text{ kg m}^{-2}$ ). RT simulations highlight the strong influence of the vertical distribution of cloud liquid water (liquid water path  $LWP < 0.1 \text{ kg m}^{-2}$ ) on the TB, which in extreme cases, can fully obscure the snow scattering signal. TB variations of the same magnitude can also be caused by typical variations in SSD parameters and particle shape similar to results obtained by space-borne studies. Ground-based stations with their infrastructural capabilities in combining active and passive microwave observations have the potential to disentangle the influences of different snow shape, SSD, and SWP in snow retrievals, thus supporting current and future satellite missions.

**Citation:** Kneifel, S., U. Löhnert, A. Battaglia, S. Crewell, and D. Siebler (2010), Snow scattering signals in ground-based passive microwave radiometer measurements, *J. Geophys. Res.*, 115, D16214, doi:10.1029/2010JD013856.

### 1. Introduction

[2] Snow is the predominant type of precipitation in sub-polar and polar latitudes [e.g., Ellis *et al.*, 2009] and plays an important role in the hydrological cycle. In polar regions, frozen precipitation determines the mass balance of the polar ice sheets. The accumulated snow on the ground is important for management of water resources, for the prediction of severe flooding when melting occurs as well as for the Earth's energy balance through the surface albedo change.

[3] In general, snow, graupel, and hail are understood as the precipitating part of cloud ice, which means the total mass of frozen hydrometeors. The distinction to nonsedimentating

cloud ice, however, is not clearly defined as discussed by Waliser *et al.* [2009], who show that for selected atmospheric models the fraction of nonsedimentating cloud ice can range between 10% and 30% of the total ice. Cloud ice is found to consist of a large variety of different sizes and shapes. The conversion mechanisms, e.g., from pristine ice crystals to aggregated snow or the interaction of cloud ice with the liquid phase is still poorly understood. The very complex microphysics of frozen hydrometeors are one reason for the enormous uncertainties in predicting cloud ice with numerical weather prediction and climate models [e.g., Stephens *et al.*, 2002; Waliser *et al.*, 2009]. For example, the prediction of total cloud ice by global circulation models deviate currently by a factor of 20 [Waliser *et al.*, 2009]. In general, the uncertainty in the prediction of precipitating cloud ice, i.e., basically snow and graupel, is even larger, because additional assumptions about the sedimentation and aggregation processes have to be made. Recently, more sophisticated ice microphysics parameterizations for a prognostic calculation of the ice water content (IWC) and even higher moments

<sup>1</sup>Institute for Meteorology and Geophysics, University of Cologne, Germany.

<sup>2</sup>Earth Observation Science, University of Leicester, United Kingdom.

<sup>3</sup>Deutsches Zentrum für Luft- und Raumfahrt, Institut für Physik der Atmosphäre, Oberpfaffenhofen, Germany.

[Lynn *et al.*, 2005; Seifert and Beheng, 2006] have been developed that are expected to better represent the large number of degrees of freedom.

[4] Obviously, observational data for model evaluation and improved understanding of the ice microphysics are strongly needed. In situ measurements of ice clouds are provided by airborne observations that give an insight into microphysical processes and the variability of particle shapes and size distributions for different cloud systems [e.g., Heymsfield *et al.*, 2002; Field *et al.*, 2005]. However, for model evaluations on a global scale, satellite observations are essential and only recently available [Liu, 2008a]. While visible and infrared satellite remote sensing observations have been available for decades and have been widely used to investigate cirrus clouds, they show poor accuracy for clouds with high amounts of integrated ice water path (IWP). In fact, visible and infrared techniques tend to be most sensitive to the cloud top because of their intrinsic incapability of sounding deeply within the cloud structure. For this reason, many efforts have focused on passive and active microwave (MW) techniques for the observation of snow, but only for the last few years, observational data have been made available on a global scale.

[5] Since 2006 vertically resolved reflectivity data from the nadir-viewing 94 GHz cloud profiling radar on the CloudSat satellite are available [Stephens *et al.*, 2002] that allow to derive vertical profiles of IWC. Passive observations at atmospheric window channels (e.g., 89 and/or 150 GHz) are provided by the advanced microwave sounding units-B onboard the NOAA-15 satellite and the Advanced Microwave Scanning Radiometer-EOS onboard the NASA Aqua satellite. Thick ice and snow clouds were found to reduce the brightness temperature (TB) signal of the Earth's upwelling thermal radiation at frequencies greater than  $\sim 90$  GHz [e.g., Katsumata *et al.*, 2000; Bennartz and Petty, 2001; Bennartz and Bauer, 2003]. This TB depression is caused by the increase of scattering by frozen hydrometeors with increasing frequency and hydrometeor size. Thus, the scattering effects can be used to derive integrated snow water path (SWP) [e.g., Noh *et al.*, 2006] but are not able to provide any information about vertical ice distribution. The passive sensors and radar data were thus combined [Skofronick-Jackson *et al.*, 2003; Evans *et al.*, 2005; Seo and Liu, 2005; Noh *et al.*, 2006; Grecu and Olson, 2008] to develop retrievals for snowfall parameters like snowfall rate, snow water content (SWC), and snow size distribution (SSD).

[6] Any snow retrieval is based on assumptions about crystal habit and SSD that have a large impact on the radiative properties and hence the quality of the retrieval. While in the past, it was common to use spheroids composed of an ice-air mixture [e.g., Skofronick-Jackson *et al.*, 2003; Hogan *et al.*, 2006] several studies started to replace spherical approximations by more realistic ice crystals like hexagonal columns, plates, rosettes, or dendrites [e.g., Evans *et al.*, 2005; Seo and Liu, 2005; Noh *et al.*, 2006; Grecu and Olson, 2008]. Observations, however, revealed [e.g., Heymsfield *et al.*, 2002; Brandes *et al.*, 2007] that natural snow also contains large amounts of aggregate habits. Currently, only a few studies [Ishimoto, 2008; Petty and Huang, 2010] started to investigate the scattering properties of large aggregate snowflakes; however, their impact on snow retrievals still remains an open question. Another source of uncertainty is the presence of supercooled liquid water that is found in ice

clouds even at very low temperatures [e.g., Boudala *et al.*, 2004]. In particular, higher MW frequencies are affected as both, snow scattering, and liquid water emission increase with frequency. An additional difficulty in deriving the liquid water contribution is due to the poor knowledge of the refractive index of supercooled liquid water. Partly because laboratory measurements for liquid water at low temperatures are extremely rare [Ellison, 2006], mass absorption coefficients, calculated by different models [Ray, 1972; Liebe *et al.*, 1991; Stogryn *et al.*, 1995; Ellison, 2006] deviate at 31.4 GHz and 0°C by about 5% and the spread increases up to 50% at  $-30^{\circ}\text{C}$ . Similar differences occur at higher frequencies (90 and 150 GHz).

[7] As an addition to global satellite observations, ground-based observations can provide long-term data of the vertical column at a fixed site. Within the “towards an optimal estimation based snowfall characterization algorithm” (TOSCA) campaign, ground-based data of snowfall from a unique combination of remote sensing and in situ measurements were collected. The remote sensing instrumentation combined active radar systems at 24 and 35 GHz with passive microwave observations in the frequency range from 20 to 150 GHz. The data set was complemented by optical disdrometers, nearby radiosonde ascents and several standard meteorological measurements. This data set can be used to investigate sensor synergies and to develop retrievals that can yield optimum strategies for space-borne sensors. Ground-based passive and active observations have the important advantage in comparison to airborne and space-borne missions, of being much less influenced by surface reflections and changing surface emissivities. With ground-based microwave radiometers (MWR), especially at the higher frequencies 90 and 150 GHz, we expect, in contrast to the previously mentioned TB depression, that the scattering effects in the upward looking geometry will produce a TB enhancement. This enhancement is caused by the snow crystal scattering of the upwelling radiation (surface emission) and is significant at frequencies larger than 90 GHz. To our knowledge, these effects have not yet been investigated for the quantitative estimation of snow microphysics.

[8] This study exploits the unique TOSCA data set with a focus on the passive microwave observations. Cloud radar reflectivity profiles provide information about the vertical distribution and temporal variability of snow. Ground-based observations with the 2-D video disdrometer (2DVD) allow us to derive the SSD and provide information about snow shape. The multispectral passive measurements enable us to distinguish between the different contributions of cloud liquid water emission and snow scattering to the total signal. Together with a radiative transfer model, we use these multispectral measurements as a test bed for our microphysical assumptions to give answers to the following main scientific questions: (1) Is it possible to observe the theoretically proposed snow scattering signal as a TB enhancement in the ground-based MW measurements and if yes, what is the magnitude of those signals and are they similar to model simulation results? (2) How do the scattering signals depend on variations in the different microphysical parameters like SWP, liquid water path (LWP), SSD, and snow shape?

[9] The paper is structured as follows: In section 2 we shortly describe the measurement campaign, the deployed instrumentation, and the applied retrieval methods. The

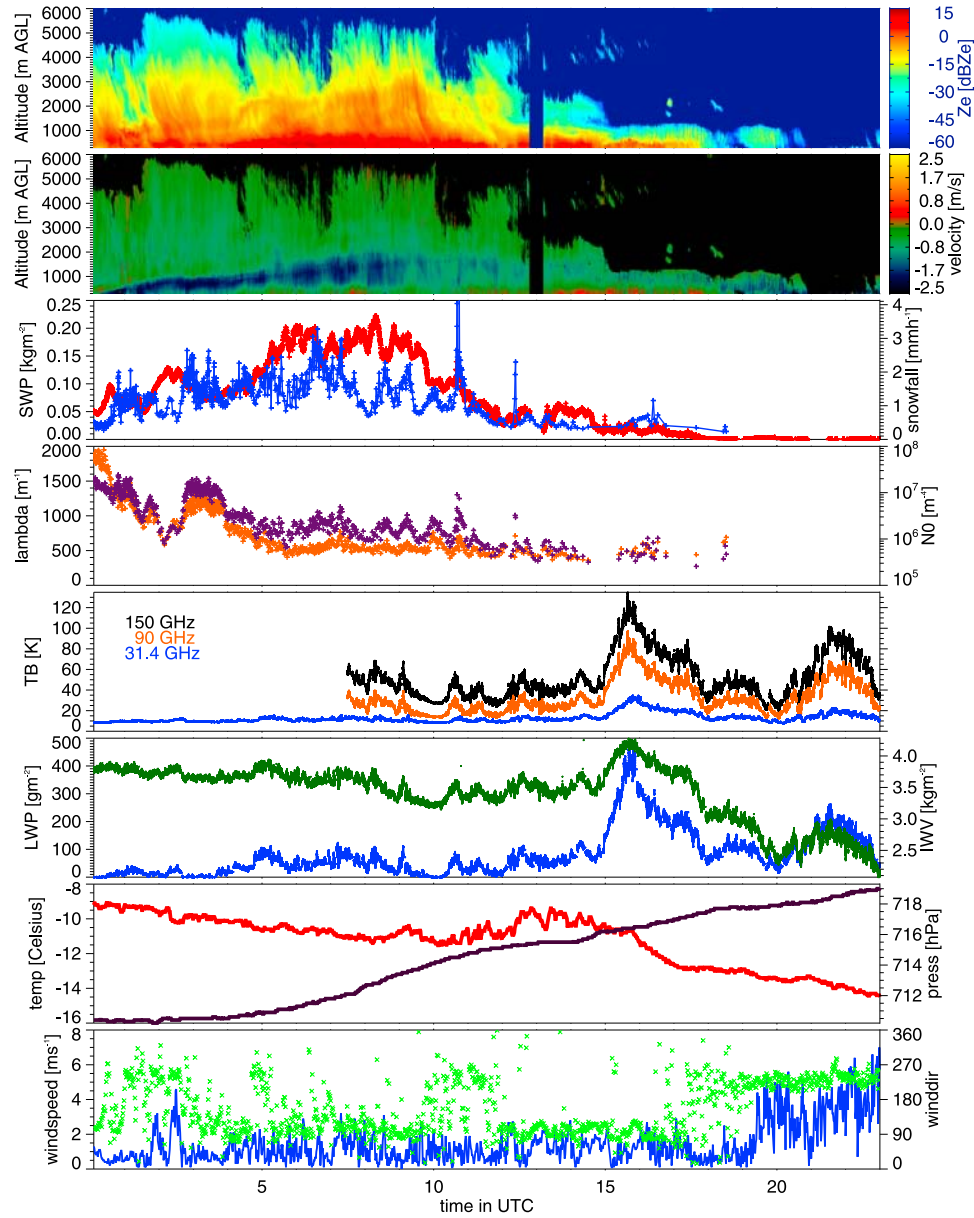


**Figure 1.** Selected measurements from a strong snow event on 8 February 2009. From the top frame, equivalent K<sub>a</sub>-band radar reflectivity in dBZe; radar Doppler velocity in ms<sup>-1</sup> (negative values = toward the radar); radar-derived snow water path in kgm<sup>-2</sup> (red); 2DVD liquid equivalent snowfall rate in mmh<sup>-1</sup> (blue); N<sub>0</sub> in m<sup>-4</sup> (orange) and λ in m<sup>-1</sup> (violet) for exponential snow size distribution (SSD) from 2DVD; MWR brightness temperatures at 150 (black), 90 (orange), and 31.4 (blue) GHz in K; IWV in kgm<sup>-2</sup> (green) and LWP in gm<sup>-2</sup> (blue) derived from HATPRO; temperature in °C (red); and air pressure in hPa (black), windspeed in ms<sup>-1</sup> (blue), and direction in degree (light green).

radiative transfer (RT) model and the sensitivity of the different microphysical parameters on the MWR signal are discussed in section 3. To compare our model sensitivities with real measurements, we analyze in section 4 a case study with focus on a 5 h snow event produced by a stratiform cloud system. In section 5 the atmospheric reconstruction as input for the RT model, the comparison of the observed MW signal with simulations together with a discussion about the remaining uncertainties are described. Because the influence of snow habit and SSD is of particular interest, the representativity of the idealized snow particles

is discussed together with the video disdrometer measurements in Appendix A. Finally, in section 6 we expand the theoretical analysis to higher MW frequencies combined with active radar systems and investigate their potential for separating information on different snow shape, SSD, and total snow water path for future snow retrieval development.

## 2. Instrumentation and Methods

[10] During TOSCA a comprehensive set of ground-based instrumentation has been deployed at the Environmental

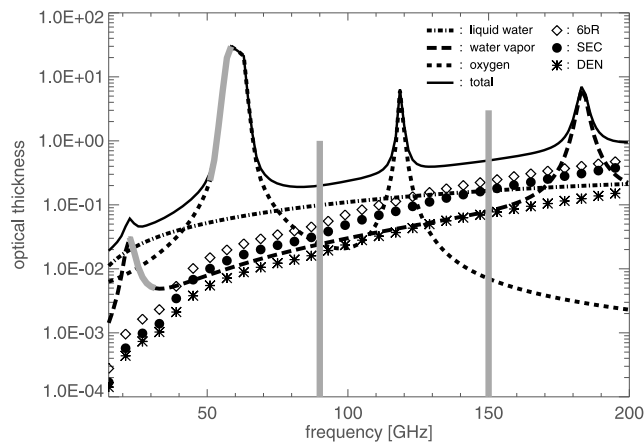


**Figure 2.** Model results for the atmospheric conditions at 8 February 2009, 08:20 UTC: single layer cloud with homogenous distributed LWP =  $0.1 \text{ kg m}^{-2}$  and SWP =  $0.2 \text{ kg m}^{-2}$ . Optical thickness is shown against frequency (GHz) for different atmospheric gases and hydrometeors: oxygen (dotted), water vapor (long dashes), liquid water (dash-dotted), and total of gaseous contributions (solid). The results for different snow shapes are indicated with symbols: 6b-rosettes (diamonds), sector snowflakes (circles), and dendrites (asterisks). The MWR frequency bands are shown by thick solid gray lines: 22.24–31.4 GHz (M1), 51.26–58.0 GHz (M2), 90 GHz and 150 GHz.

Research Station Schneefernerhaus (UFS at 2650 m mean sea level, MSL; Lat.:  $47^{\circ}25'N$ , Lon.:  $10^{\circ}59'E$ ) at the Zugspitze Mountain, Germany, in the winter season 2008–2009. A detailed description of the project and the instrument specifications are available at <http://gop.meteo.uni-koeln.de/tosca>. The UFS offers an excellent infrastructure with laboratories and observational and experimental decks to the national and international scientific community. UFS is ideally located for snow observation because of the frequent occurrence of snowfall and the presence of low water vapor amounts (typically integrated water vapor (IWV)  $< 6 \text{ kg m}^{-2}$  during wintertime). The latter is of interest because the dry atmospheric conditions provide a cold background for scattering signals originating from ice hydrometeors although saturation effects at 90 and 150 GHz become dominant only at IWV values larger than  $25 \text{ kg m}^{-2}$ . During TOSCA, the standard instrumentation (i.e., wind speed and direction, temperature, humidity, etc., measured by the German Weather Service) was significantly enhanced to provide an excellent overview on snow characteristics as illustrated for a strong snowfall case on 8 February 2009 (Figure 1).

## 2.1. Cloud Radar

[11] The vertical distribution of hydrometeors, their Doppler fall velocities, and their linear depolarization ratio is observed by a Metek Ka-band (35.5 GHz) cloud radar [Melchionna *et al.*, 2008]. The system has a range resolution of 30 m and a sensitivity of  $-44 \text{ dBZ}$  at 5 km range. The lowest-range gate is limited to 300 m making the combination with a Lidar ceilometer useful to improve the cloud base detection. To derive vertical profiles of snow water content from radar reflectivities, a large variety of different

Z-SWC relationships has been proposed. Similar to Z-snow rate relations [e.g., Kulie and Bennartz, 2009], those Z-SWC relations are extremely dependent on the assumed snow shape and size distribution. In the worst case, the derived SWC values can deviate from each other by some orders of magnitude (M. Kulie, personal communication, 2010). Here we apply the temperature dependent method described by Hogan *et al.* [2006] for the radar-based estimation of SWP (height-integrated SWC). The temperature dependence takes into account that the SSD broadens when the initial ice crystals fall through the cloud. At the cloud top (low temperatures) the SSD is narrow, while with increasing distance from the top diffusional growth and aggregation lead to larger structures. It has to be noted that the difficult distinction between precipitating ice (snow, graupel, hail) and nonsedimentating cloud ice often leads to the similar use of the terms ice water (IWC/IWP) and snow water (SWC/SWP). Sometimes ice is also defined as idealized pristine crystals, whereas snow is basically assumed to consist of aggregates. To avoid confusion, we will use the term SWC/SWP instead of IWC/IWP in the following because in our definition snow includes both idealized ice crystals and aggregates.

## 2.2. Passive Microwave Radiometers

[12] Two passive microwave radiometers manufactured by Radiometer Physics GmbH (RPG) were deployed: a Humidity and Temperature Profiler (HATPRO) [Rose *et al.*, 2005] and the Dual Polarization Radiometer (DPR) [Turner *et al.*, 2009], comprising a total of 17 channels in the frequency range from 22 to 150 GHz. The microwave profiler HATPRO was designed as a network-suitable low-cost radiometer, which can observe LWP, humidity, and temperature profiles with high temporal resolution up to 1 s. HATPRO consists of total-power radiometers utilizing direct detection receivers within two bands, M1 (22.235–31.4 GHz) and M2 (51.26–58.0 GHz) (Figure 2). The seven channels of band M1 contain information on the vertical profile of humidity through the pressure broadening of the optically thin 22.235 GHz  $\text{H}_2\text{O}$  line, and therefore also about the IWV. Simultaneously, LWP can be derived from cloud water emission, which increases with frequency (Figure 2). Using multilinear regression [Löhnert *et al.*, 2001], IWV and LWP can be derived with accuracies better than  $0.7 \text{ kg m}^{-2}$  and  $20 \text{ g m}^{-2}$ , respectively. The seven channels of band M2 contain information on the vertical profile of temperature because of the homogeneous mixing of  $\text{O}_2$  throughout the atmosphere. At the opaque center of the  $\text{O}_2$  absorption complex at 60 GHz, most of the information originates from near the surface, whereas further away from the line, the atmosphere becomes less opaque, so an increasing amount of information also originates from higher atmospheric layers.

[13] The DPR is a three-channel system that performs observations at the window frequencies 90 and 150 GHz, also frequently used by satellite instruments. It uses direct detection at 90 GHz, whereas the 150 GHz channels are heterodyne systems. A wire grid is used to separate the polarizations at the latter frequency so both the vertical and horizontal polarization can be measured separately and simultaneously. To conserve the plane of polarization during

elevation scanning, the DPR is mounted on a rotating horizontal axis.

[14] Both radiometers are occasionally calibrated by viewing a liquid nitrogen target and the observations from this target and the internal blackbody are used to determine the noise source temperature (in case of HATPRO), system noise temperature, and the gain. Because the noise source and the system noise temperature are assumed to be highly stable, RPG recommends liquid-nitrogen calibration at the beginning of a deployment and every few months after that. However, the gain is updated every few minutes by interrupting the atmospheric observations and viewing an internal blackbody target at ambient temperature. HATPRO also performed regularly scheduled tipping scans [Han and Westwater, 2000], for its channels in the range from 22.24 to 31.4 GHz. These were automatically evaluated by the operational radiometer software to update the calibration in case the sky was determined to be homogeneous and cloud free.

[15] To ensure a high quality of the measured MWR data, it is essential not only to have precise calibrations but also to keep the radome completely free of liquid or frozen water. For that purpose, both radiometers are equipped with heated blower systems. However, under rough weather conditions, like heavy snowstorms or strong rain, these systems reach their limits. To quality control the data and thus to flag disturbed data, two cameras were installed for permanent observation of the radome conditions. For this study, only data that passed a visual inspection have been used.

### 2.3. Two-Dimensional Video Disdrometer

[16] The 2DVD [Kruger and Krajewski, 2002] developed by Joanneum Research supplied important information about shape and intensity of snowfall close to the ground. In contrast to standard optical disdrometers, the 2DVD illuminates the hydrometeors with two cameras from two orthogonal sides allowing the determination of size, shape, and fall velocity of the particle. Large ambient wind speeds have been identified by Nešpor *et al.* [2000] and Brandes *et al.* [2007] to be responsible for potential undersampling particularly of smaller particles. To exclude 2DVD data possibly disturbed by wind effects, we only consider 2DVD measurements in low wind speed conditions ( $v < 5 \text{ ms}^{-1}$ ). We assume an exponential SSD

$$N(D) = N_0 \cdot \exp(-\lambda D), \quad (1)$$

with  $N(D)$  ( $\text{m}^{-4}$ ) as the particle number density in a given particle size range,  $N_0$  ( $\text{m}^{-4}$ ) as the intercept parameter, and  $\lambda$  ( $\text{m}^{-1}$ ) as the slope coefficient. From the two 2DVD views of the particle, we select first the image with the largest particle extension and then define the maximum particle dimension  $D$  as the largest axis of the circumscribed ellipse. To estimate the two parameters  $N_0$  and  $\lambda$  for the SSD, it is important (1) to have a sufficient large sample size [Smith and Kliche, 2005] and (2) to ensure that the sample originates from a single SSD, i.e., the same microphysical process, requiring a sufficiently short time period. As a compromise between both demands, we calculate  $N_0$  and  $\lambda$  with the moment method described in, e.g., Field *et al.* [2005] for every 1000 particles within a maximum allowed time period of 5 min. Measurement periods that do not

satisfy these criteria are not considered for the SSD, and hence the temporal density of 2DVD data points in Figure 1 changes during time. We also excluded those snow particles with unrealistically high fall velocities of  $>4 \text{ ms}^{-1}$  and height to length ratios lower (greater) than 0.1 (10) that are probably artificially generated by the 2DVD software because of wrong particle image matching [Hanesch, 1999].

[17] From the approximated particle volume provided by the 2DVD software [e.g., Brandes *et al.*, 2007] and a density, maximum size relation [Muramoto *et al.*, 1995], it is further possible to calculate a liquid equivalent snowfall rate (Figure 1, third frame). Because the particle volume approximation is based on only two projections, it cannot fully account for the “fluffiness” of the snow aggregates, and hence, the derived snowfall rate should be interpreted with care.

## 3. Radiative Transfer

### 3.1. Model Description

[18] The radiative transfer calculations are obtained by using the RT3 model [Evans and Stephens, 1991]. It simulates the thermal radiation field within a medium of randomly oriented particles. In the following subsections, the model input fields and the employed models of absorption and scattering properties for different gases and hydrometeors are described.

#### 3.1.1. Surface Emissivity

[19] The ground is treated as a Lambertian surface. This assumption is backed by experimental observations of snow-covered land surfaces [e.g., Hewison and English, 1999, Figure 5]. Surface emissivity strongly depends on frequency and snowpack properties. A surface covered by fresh snow has very high emissivity ( $>0.9$ ) at frequencies from 24 to 150 GHz, while crusty snow can have low emissivity values at high frequencies (e.g., even below 0.5 above 90 GHz) [Yan *et al.*, 2008, Table 4]. A layer of deep dry snow has values in-between, with 0.6–0.7 being typical values at 90 and 150 GHz. In this study we assume a constant surface snow emissivity of 0.9 according to fresh snow because we concentrate on a long-lasting snow event with continuous snowfall and low temperature variations. In general, the surface emission variability (if not accounted for) can contaminate the TB signal from the atmospheric falling snow and can cause errors in the retrievals. This problem strongly affects satellite radiometric measurements [Skofronick-Jackson *et al.*, 2004; Noh *et al.*, 2009] but has an impact to ground-based measurements as well: the higher the ground emissivity the stronger the upwelling radiation leaving the surface and the larger the radiation scattered back to the ground by the snow. To quantify this effect, we have performed a RT sensitivity study by modeling a snowfall event with SWP values up to  $0.4 \text{ kg m}^{-2}$ , different SSDs (similar to section 6), and a changing surface emissivity from 0.9 to 0.5. The derived differences between simulated downwelling TBs at the ground are lower than 10 K for 150 GHz and lower than 5 K for 90 GHz. Although the absolute differences are lower at 90 GHz because of the lower amount of scattering at snowflakes, the sensitivity to different emissivities is in general greater at lower frequencies.

**Table 1.** Parameters for the Mass-Size Relation<sup>a</sup> and Largest Maximum Diameter  $D$  for the Different Snowflake Types Derived From the Liu Database

Particle type	a	b	largest $D$ [mm]
6b-rosette	0.2124	2.285	10
Sector snowflake	$1.191 \cdot 10^{-3}$	1.511	10
Dendrite	$5.666 \cdot 10^{-3}$	1.820	12.454

<sup>a</sup>Equation (2), SI units; Liu [2008b].

### 3.1.2. Gas Absorption

[20] The absorption of gases in the microwave region is modeled using the formulation of *Rosenkranz* [1998], which accounts for the absorption by  $H_2O$ ,  $O_2$ , and  $N_2$  gases. The line width modification according to the HITRAN database of the 22.235 GHz  $H_2O$  line as proposed by *Liljegren et al.* [2005] has been taken into account.

### 3.1.3. Liquid Water

[21] Cloud droplets are assumed to be monodispersely distributed with a radius of 10  $\mu m$ , and their emission is calculated using Mie theory. The liquid water refractive index was simulated with a recent model from *Ellison* [2006]. It is important to note that the modeled values of the refractive index for supercooled water in the microwave region are primarily based on extrapolations from higher-temperature regions. Because only laboratory measurements for supercooled water exist at 9.6 GHz [*Bertolini et al.*, 1982], a large frequency and temperature range has not been verified by measurements and should be interpreted with care. We did not consider any rain drops ( $r > 100 \mu m$ ) in our calculations, as all events considered had temperatures lower than  $-9^\circ C$ , and no rain could be detected by the webcam.

### 3.1.4. Snow

[22] Snow produces a strong scattering signal in the microwave region, whereas emission is nearly negligible due to the characteristic ice refractive index. The scattering signal strongly depends on the assumption of snow shape and SSD, especially at higher size parameters.

[23] In the past, snow scattering properties have often been parameterized with simple spherical particles (mass or volume equivalent with solid ice or ice-air mixture) because of the exact and cost effective calculation by Mie or T-Matrix theory. However, *Kim* [2006] showed that this approximation of snow particles with spheroids is only valid up to a size parameter  $x = 2\pi r_{\text{eff}}/\lambda$  of  $\sim 2.5$ , with  $r_{\text{eff}}$  being the radius of the solid ice mass equivalent sphere. For example, at 150 GHz, this would limit  $r_{\text{eff}}$  to 0.8 mm; therefore, this simplification is not useful for snow at high microwave frequencies and for large snowflake sizes. Recently, some single scattering databases with more realistically shaped particles like hexagonal plates, rosettes, dendrites, etc. [e.g., *Hong*, 2007; *Liu*, 2008b] were published. They consistently show that the sensitivity to shape increases both with frequency and particle size. As a consequence, several studies conclude that any approximations with spheres have difficulties to simultaneously represent all scattering properties like scattering matrix, backscattering, scattering, and extinction cross sections [*Kim*, 2006; *Petty and Huang*, 2010]. Typical pristine snow, like hexagonal columns, plates, or dendrites, are found to be only representative for the smaller end of the size spectrum. In midlatitude snowfall, ground-based in situ measurements,

e.g., with optical disdrometers [e.g., *Brandes et al.*, 2007; *Huang et al.*, 2009], suggest that larger snow mainly consists of complex aggregates without “typical” shape.

[24] Because of the strong radiative effects of large aggregate structures, first studies built models of large snowflakes based on in situ measurements. *Ishimoto* [2008] studied the backscattering properties of fractal aggregates at 9.8, 35, and 95 GHz. *Petty and Huang* [2010] performed single scattering calculations for different realistic aggregates consisting of dendrites and needles at 13.4, 18.7, 35.6, 36.5, and 89.0 GHz. Unfortunately, these results do not cover our 150 GHz measurements and to our knowledge; currently, no single scattering database for large snow aggregates ( $> 1$  cm) at microwave frequencies does yet exist.

[25] In this study we use the database developed by *Liu* [2008b], from which we chose the following snow habits for our simulations: dendrites (DEN), six bullet rosettes (6bR), and sector snowflakes (SEC) up to maximum particle sizes of  $\sim 1$  cm (Table 1). The database also contains several hexagonal plates and columns, but their maximum particle diameter  $D$  is much lower and thus less useful to simulate snowfall with a realistic spectrum of particle sizes. There are also different kinds of rosettes (3–5 bullets) available, but for this study, we chose only the six-bullet type as an exemplary “3-D particle” compared to the more “2-D” shapes SEC and DEN. Figure 3 gives an overview of the absorption and scattering and backscattering efficiencies (i.e., cross section divided by  $\pi r_{\text{eff}}^2$ ) of the four rosette types, SEC, and DEN. DEN and SEC show the lowest values for all efficiencies at every size. The 6bR approximately represent an average of the four rosette types for absorption and scattering while they produce the largest backscatter of all particle types. Hence, the three selected shapes are representative for the possible range of scattering behavior of all idealized particles in the database.

[26] To give a rough estimate of the differences between realistic aggregates and the idealized Liu particles used in this study, we compare the results from *Petty and Huang* [2010] at 89 GHz in terms of extinction per unit mass (Figure 4). We find that all Liu particles with masses lower than 0.02 mg have lower extinction values compared to aggregates. For larger masses, almost all Liu particles show extinction values higher than for aggregates. The only exception are the Liu dendrites, which agree very well with the aggregates if their mass exceeds 0.02 mg. This corresponds to a maximum dendrite size of  $\sim 1.2$  mm. However, this comparison cannot answer the question if their extinction values agree similar well at higher frequencies (e.g., 150 GHz). In Appendix A we further discuss the representativeness of the selected particle types by comparing them to shape properties of snow particles measured with the 2DVD.

[27] The particles in the database are based on certain assumptions concerning the relationship between particle mass  $m$  (kg) and maximum particle diameter  $D$  (m), which can be approximated by a power law of the form

$$m(D) = aD^b. \quad (2)$$

[28] Table 1 gives the coefficients  $a$  and  $b$  for the different snow habits together with the largest available particle diameter  $D$  as derived from the database. Besides the assumption on the single snowflake shape, the modeling of



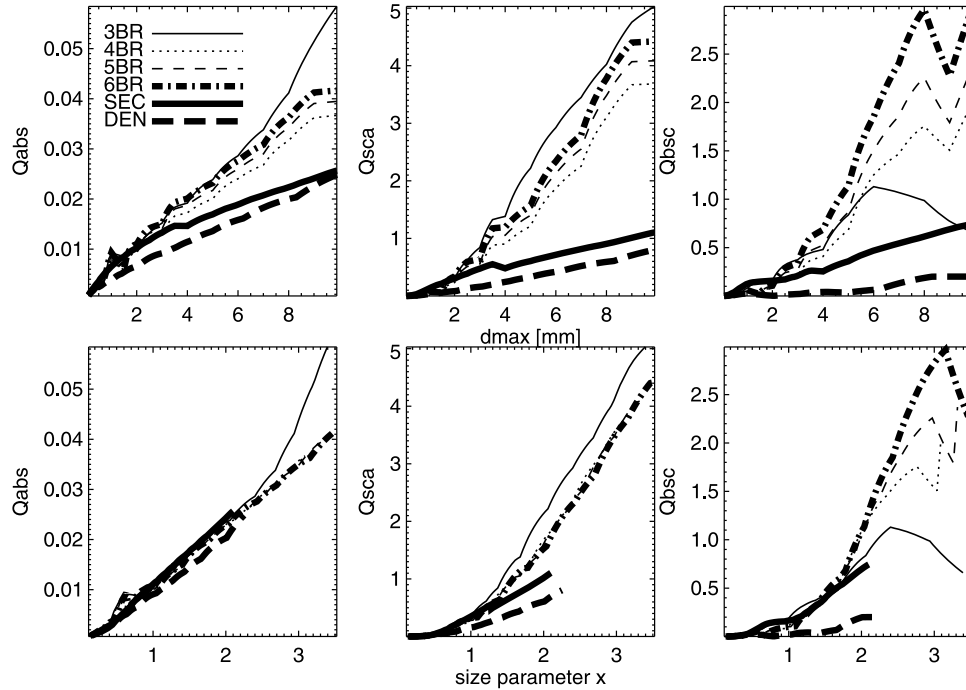


**Figure 3.** (left) Absorption, (middle) scattering, and (right) backscattering efficiencies (i.e., cross sections divided by  $\pi r_{\text{eff}}^2$ ) at 150 GHz for different idealized snow particles based on the Liu database: Rosettes (3-bullet: thin solid, 4-bullet: dotted, 5-bullet: dashed, 6-bullet: dash-dotted), sector snowflakes (thick solid), and dendrites (long dashed). (top) Scattering properties against the maximum particle diameter  $D$  in millimeter and (bottom) against the size parameter  $x$  (defined in the text).

the total scattering signal of snow clouds also depends on the SSD. Different experimental and modeling studies [e.g., *Matrosov*, 2007, and references therein] showed that an exponential distribution (equation (1)) is a good assumption for particle sizes larger than 1 mm. If SWC together with the particle's mass size relation (equation (2)) and one of the two SSD parameters  $\lambda$  or  $N_0$  are given, the other distribution parameter can be calculated by combining equations (1) and (2) to

$$\lambda = \left[ \frac{N_0 a}{\text{SWC}} \Gamma(b+1) \right]^{\frac{1}{b+1}} \quad (3)$$

with the gamma function  $\Gamma$ . From equation (3), it can be seen that increasing snow content causes the SSD to broaden, i.e., the number of large particles increases. Unfortunately, the largest available particle sizes in the database (Table 1) range from 1.0 to 1.2 cm. For all particles with diameters larger than this threshold, we use the scattering properties of the largest available particle in the database. To avoid possible TB underestimations, we calculate the maximum possible SWC for different  $N_0$  values and particle types under the restriction that 99% of the distributed snow mass is composed by particles smaller than the database size limits. For SEC and  $N_0$  of  $10^6 \text{ m}^{-4}$ , we find the smallest SWC content of  $0.094 \text{ gm}^{-3}$ , whereas for 6bR and DEN, the values are slightly higher ( $0.114$  and  $0.113 \text{ gm}^{-3}$ , respectively). Increasing  $N_0$  by a factor of 10 will enlarge the maximum possible SWC by the same factor. In the following study the SWCs are always far below the critical SWC values, and

hence, the assumed SSDs will not contain significant amounts of particles exceeding the database size limits.

### 3.2. Spectral Sensitivity

[29] Figure 2 illustrates the spectral contributions of the different atmospheric constituents to the microwave signal

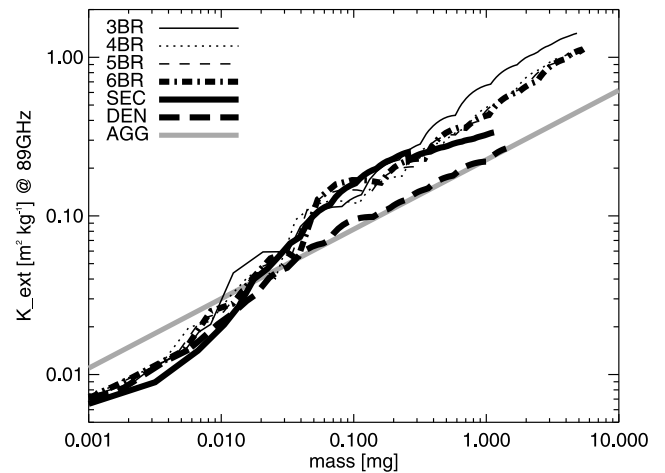


**Figure 4.** Extinction cross section divided by particle mass (mass extinction coefficient) in  $\text{m}^2 \text{kg}^{-1}$  as a function of particle mass in mg for 89 GHz and idealized Liu snow particles (line coding and description same as in Figure 3). The solid gray line represents the power law fit to four different realistic aggregate models given in the study by *Petty and Huang* [2010].

in terms of optical thickness. The calculations are carried out for the snow event on 8 February 2009, 08:20 UTC (Figure 1) that was characterized by dry conditions ( $IWV = 3.5 \text{ kg m}^{-2}$ ) and cold air temperatures ( $-11^\circ\text{C}$ ). To reproduce these conditions, we use temporal interpolated profiles of pressure, temperature, and humidity from radiosonde launch at Innsbruck and Munich and information on cloud height and thickness from the cloud radar. The 5.5 km thick single layer cloud is assumed to consist of snow particles and liquid water droplets (i.e.,  $SWP = 0.2 \text{ kg m}^{-2}$  and  $LWP = 0.1 \text{ kg m}^{-2}$ ).

[30] The frequency range from 15 to 200 GHz shows several resonant gas absorption line characteristics. The channels located in the window regions are sensitive to absorption and scattering due to hydrometeors, especially in the high Alpine UFS environment, where the contribution of the water vapor continuum absorption is very small. Liquid cloud water and snow both show a continuous increase of absorption and scattering with frequency. While the liquid water opacity is due to the temperature-dependent emission of cloud droplets, the snow opacity is mostly caused by scattering. For this particular case, the snow optical thickness is lower than the liquid water emission for all frequencies below 120 GHz. In general (e.g., for the typical range of liquid water and snow amounts), the frequency of equal optical thickness for snow and liquid water indicates that frequencies larger than 90 GHz are particularly useful for snow detection. The 6bR particle type produces the highest snow scattering signal, followed by SEC and DEN (Figure 2). The optical thickness of SEC and DEN compared to 6bR at 150 GHz is 28% and 69% lower, respectively. Moving to lower frequencies, the differences between SEC and DEN only change slightly: At 90 GHz, the relative difference to 6bR is 31% (65%) lower for SEC (DEN). Note that the spectral sensitivity of snow also depends on the SSD. These effects are discussed in detail in section 5.2.

#### 4. Case Study: 8 February 2009

[31] For a detailed analysis, we chose a day with a long-lasting snow event and temperatures between  $-9^\circ\text{C}$  and  $-15^\circ\text{C}$  at the surface (Figure 1), to make sure that melting layer effects did not influence the measurements. The data for this time period reveal the presence of supercooled liquid water in combination with snowfall, which was frequently observed during TOSCA. This allows us to investigate the influence of supercooled liquid water in combination with snow on the passive TB.

[32] The synoptic situation was characterized by two low pressure systems over Scandinavia and the northern Mediterranean Sea, respectively, leading to a weak flow from the north over the Alpine region. Both systems moved slowly eastward during the day, which caused the slight pressure increase seen in Figure 1. The first part of the day, between 00:00 and 15:00 UTC, was dominated by strong snowfall with a total snow depth increase of  $\sim 25 \text{ cm}$  (manual observation at the summit of the Zugspitze Mountain about 300 m higher than the UFS). In this time period, the air temperature decreased only slightly from  $-9^\circ\text{C}$  to  $-11^\circ\text{C}$ , while between 15 and 24 UTC, the temperature declined to  $-15^\circ\text{C}$ . The temperature change was accompanied by a decrease of the atmospheric integrated water vapor content

from 4 to  $2 \text{ kg m}^{-2}$ , interrupted by a short increase ( $\sim 1 \text{ kg m}^{-2}$ ) between 15:00 and 17:00 UTC. The LWP was below  $100 \text{ gm}^{-2}$  until 15:00 UTC and showed a strong increase up to  $450 \text{ gm}^{-2}$  at 16:00 UTC followed by a second peak of  $200 \text{ gm}^{-2}$  at 22:00 UTC. Cloud radar and ceilometer measurements revealed that those later LWP maxima were produced by shallow clouds producing only negligible amounts of snowfall. The most distinctive changes in surface wind speed and direction can be seen after 15:00 UTC, when wind speed increased from  $1\text{--}3 \text{ ms}^{-1}$  to  $3\text{--}6 \text{ ms}^{-1}$  after 19:00 UTC and the wind direction changed from fluctuating easterly to westerly direction. In brief, the standard meteorological parameters like temperature, humidity, and wind speed indicate changing air masses especially around 15:00 UTC.

[33] Considering the vertical hydrometeor distribution, the radar shows a mainly stratiform snow cloud with some remarkable structures: The cloud radar measured the cloud tops at 3–5.5 km altitude from 00:00–12:00 UTC while they decreased down to 1–2.5 km from 12:00–18:00 UTC. The cloud bottom was detected by the ceilometer in the lowest layer; also, the webcam observations clearly indicate a cloud at ground level. In the first period from 01:00 to 12:00 UTC, the Doppler velocity from the  $K_a$ -band cloud radar shows a region with enhanced fall velocities of  $2.5 \text{ ms}^{-1}$  slightly moving to higher altitudes with time. Because riming is known to strongly influence the fall velocity of snow particles, these higher fall velocities could be evidence for the presence of supercooled liquid in that cloud region [Zawadzki *et al.*, 2001]. The radar derived SWP values (Figure 1, third frame) range between 0.05 and  $0.23 \text{ kg m}^{-2}$  in the most active snow period from 00:00 to 13:00 UTC. The contribution of cloud droplets to the radar reflectivity signal is negligible compared to the contribution of snow: For an equal SWC/LWC of  $1 \times 10^4 \text{ kg m}^{-3}$  (e.g.,  $SWP/LWP = 0.1 \text{ kg m}^{-2}$  distributed over a 1 km thick cloud), the reflectivities would be  $-35 \text{ dBZ}$  for liquid cloud water and  $\sim 10 \text{ dBZ}$  for snow (depending on shape and SSD assumptions). Therefore, the influence of liquid water on the observed SWC is lower than 1% and therefore significantly lower than other uncertainties in Z-SWC relations.

[34] Similar to the radar data, the liquid equivalent snowfall rate derived from 2DVD measurements reveal the strongest snow activity between 00:00 and 13:00 UTC with maximum snow rates of  $1.2 \text{ mm h}^{-1}$  (Figure 1, third frame). Radar-derived SWP values and 2DVD snowfall rate show some structural agreement, e.g., in the increasing snow activity from 00:00 to 08:00 UTC. It is, however, difficult to directly compare these variables because of the large uncertainties in both, the radar Z-SWC relations and the 2DVD derived snow rates as well as wind shear effects, which always cause spatial and temporal shifts.

[35] The time series of the passive MWR brightness temperatures (TB) for the frequencies 31.4, 90, and 150 GHz (Figure 1, fifth frame) represent a superposition of signals from liquid water, snow particles, water vapor, and temperature. Thus, in general, no simple estimation of hydrometeor contents can be made from the passive microwave measurements alone. Unfortunately, no DPR data (90 and 150 GHz) are available before 07:30 UTC due to software problems, whereas HATPRO data exist for the whole day. As mentioned earlier in section 2, HATPRO's low-frequency



channels (22–31 GHz) can be used to retrieve integrated values of liquid water and water vapor (Figure 1, sixth panel). The influence of snow scattering on the total signal is lower than 0.5 K for SWP values below  $0.2 \text{ kg m}^{-2}$  and therefore within the instrument noise level. In combination with the cloud radar and 2DVD observations, we are able to identify the significant TB enhancements at 90 and 150 GHz around 15:00 and 22:00 UTC, of mainly being liquid water signals originating from very shallow cloud structures (cloud tops < 1 km) with almost negligible amounts of snowfall at ground level.

[36] The DPR additionally provides information on both horizontal and vertical polarizations at 150 GHz (not shown). If snowflakes fall in an oriented manner, snow scattering should lead to marked polarization differences as a function of zenith angle. For example, *Troitsky et al.* [2003] reported polarization differences at a zenith angle of  $65^\circ$  of 2–4.5 K at 85 GHz and 2.5 K at 37 GHz for their ground-based MW measurements in winter mixed phase clouds. Contrastingly, our polarization differences at 150 GHz within the selected time period and at zenith angles between  $15.6^\circ$  and  $90^\circ$  were found to be lower than the instrument's noise level of  $\pm 0.6$  K. On the basis of these results, we conclude for the investigated snow case that snowflakes are not significantly oriented, and thus, the model assumption of randomly oriented snow particles is reasonable.

[37] On the basis of the available measurements, we reconstructed the state of the atmosphere during the snow event (10 min temporal resolution) as good as possible. Because of lack of better knowledge, several realistic scenarios for snow crystal properties were generated and used as RT model input in an effort to constrain the snow characteristics.

## 5. RT Model Results for 8 February 2009

### 5.1. Reconstruction of the Atmospheric State

[38] Atmospheric profiles and cloud structures used for the RT model input are mainly derived from radiosonde ascents (RS) and cloud radar measurements. We use RS ascents from Munich (00:00, 12:00, 24:00 UTC, distance  $\sim 90$  km; height, 489 m MSL) and Innsbruck (03:00 UTC, distance  $\sim 30$  km; height, 593 m MSL) to reconstruct the profiles of temperature, humidity, and pressure.

[39] For this purpose the different RS measurements above the UFS station height (i.e., 2650 m MSL) were interpolated to 10 min time intervals. This simple procedure is justified because UFS was located above the atmospheric boundary layer, and horizontal gradients were weak during the investigated time period. With the RS profiles, we are able to resolve the finer vertical structure, which is difficult to resolve using HATPRO retrievals. On the other hand, HATPRO can provide IWV measurements with relatively high accuracy (better than  $0.7 \text{ kg m}^{-2}$ ) and fine temporal resolution. Thus, we scale the humidity profiles with the 10 min averaged IWV derived from HATPRO to combine the RS highly resolved vertical structure with the high temporal resolution of HATPRO.

[40] For the RT simulations, reasonable assumptions about the profiles of SSD parameters ( $\lambda$  and  $N_0$ ) and particle shape have to be made. Equation (3) illustrates that if SWC,

particle shape, and one of the SSD parameters ( $\lambda$  or  $N_0$ ) are known, the remaining parameter can be calculated. Assuming a vertically constant intercept parameter  $N_0$  (i.e., from the 2DVD, section 2) and a certain particle type, the radar-derived SWC constrains the slope parameter  $\lambda$ . It should be noted that the Z-SWC relation is based on scattering calculations of ice-air spheres [*Hogan et al.*, 2006] unlike the more realistic pristine crystals used for the MW RT here. However, the comparison of their Z-SWC relation with relations derived for the Liu particle shapes reveals that it falls well within the uncertainty range induced by the different Liu particles. The assumption of a vertically constant  $N_0$  is somewhat simplifying because aircraft studies revealed a temperature dependence [e.g., *Field et al.*, 2005] most likely due to the temperature dependent aggregation processes. Hence, the values for  $N_0$  would vary between  $2.2 \times 10^7$  and  $9.4 \times 10^8 \text{ m}^{-4}$  in the temperature range from  $-10^\circ\text{C}$  to  $-45^\circ\text{C}$ .

[41] Because the definition of appropriate snow habits is difficult, the simulations were performed for the three idealized snow habits (6bR, SEC, and DEN) described in section 3.1. The induced uncertainty range is assessed in Appendix A by a comparison of the idealized shape properties with the 2DVD measurements. The time series of SSD parameters, derived by the method described in section 2, show the highest values for  $N_0$  and  $\lambda$  during the morning hours (00:00–05:00 UTC) with  $1 \times 10^6$ – $2 \times 10^7 \text{ m}^{-4}$  and  $8 \times 10^2$ – $2 \times 10^3 \text{ m}^{-1}$ , respectively. After 05:00 UTC, both parameters remain at relatively low values of  $2 \times 10^5$ – $8 \times 10^6 \text{ m}^{-4}$  for  $N_0$  and  $3$ – $8 \times 10^2 \text{ m}^{-1}$  for  $\lambda$  indicating broader SSDs with large particles. The observations are compared with the temperature-dependent parameterization (equation (4)) from *Field et al.* [2005]

$$N_0 = 7.63 \times 10^6 \exp(-0.107T_c), \quad (4)$$

with the cloud temperature  $T_c$  in degree Celsius, frequently used in numerical weather prediction models.  $N_0$  should thus vary between 2.0 and  $3.4 \times 10^7 \text{ m}^{-4}$  in the temperature range from  $-9^\circ\text{C}$  to  $-14^\circ\text{C}$  (taking the air temperature at ground for  $T_c$ ). The measured values for  $N_0$ , however, are between  $2 \times 10^5$  and  $2 \times 10^7$  and hence significantly lower compared to the Field parameterization, which is based on a large data set of aircraft measurements. *Field et al.* [2005] defined  $D$  as the particle size parallel to the flight direction. Because of the measurement system, the usable size range is limited to 0.1–4.4 mm. In contrast, we derive  $D$  from the 2DVD's two particle projections and consider particle sizes from 0.5 to 40 mm. Because of these differences in the measurement system and the definition of  $D$ , a direct comparison is difficult. *Heymsfield et al.* [2008] also mentioned shattering effects of large snowflakes at the optical aircraft probe, which lead to artificially higher (lower) numbers of small (large) particles. Another explanation for the deviations in  $N_0$  might come from the special orographic conditions at the UFS. *Kusunoki et al.* [2005] reported increasing snow aggregation because of stronger upwinds and turbulence in a mountainous orography. These larger particles would consequently result in lower values for  $N_0$  and  $\lambda$ , i.e., a broader SSD.

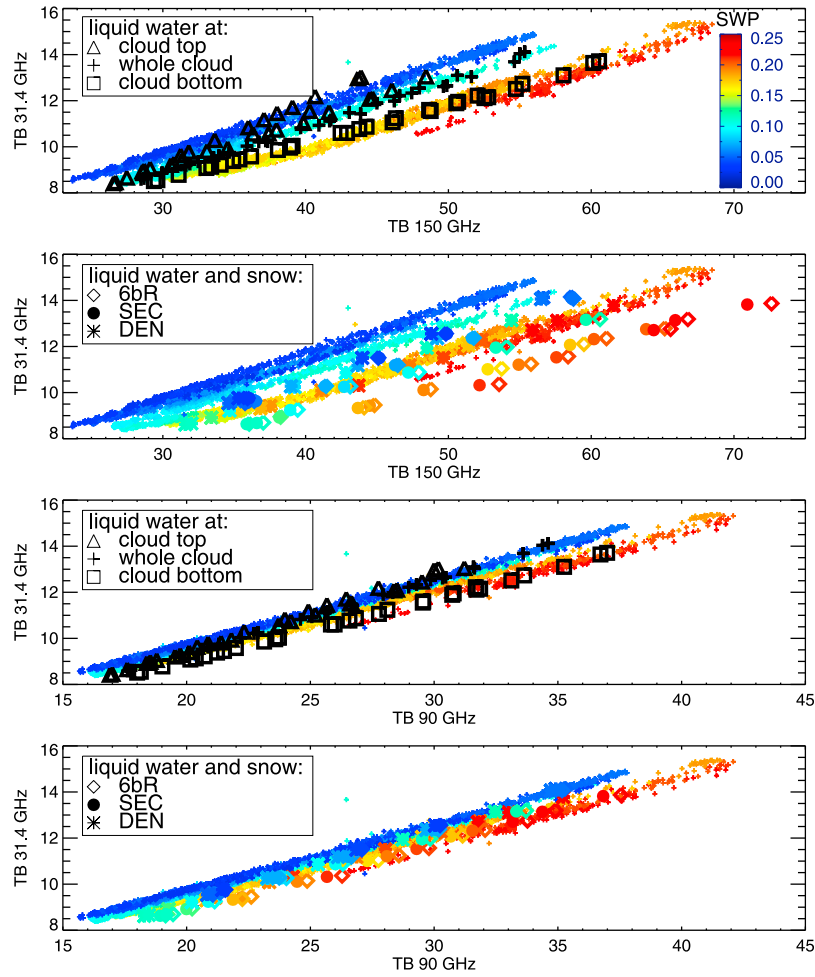


**Figure 5.** Comparison of measured and modeled TB from 8 February 2009, 07:30–12:40 UTC. The two top frames show the frequency combination 31.4/150 GHz, whereas the two bottom frames are for 31.4/90 GHz. The small symbols represent the measurements by the two MWR at a 1 s time resolution. The color shows the SWP in  $\text{kgm}^{-2}$  derived from 35 GHz cloud radar measurements. Large symbols show model simulation results for 10 min averaged atmospheric input fields (details see text). Black symbols correspond to simulations with only cloud liquid water (HATPRO-derived LWP:  $0\text{--}100\text{ gm}^{-2}$ ) at different cloud positions: cloud top (triangles), cloud bottom (squares), and homogeneously distributed over the total cloud (plus signs). The large colored symbols show the simulations for the scenario of homogeneously distributed liquid water together with snow for  $N_0 = 1 \times 10^7\text{ m}^{-4}$  and three different snow shapes: 6bR (diamonds), SEC (circles), and DEN (asterisks).

## 5.2. Model Comparison

[42] In this subsection we investigate the potential of multispectral microwave radiometry to distinguish between liquid water and snow signals. In our simulation study we focus on the time period 07:30–12:40 UTC when the largest amounts of snowfall occurred and all MWR measurements were available. Because hydrometeor signals are most evident at window frequencies (Figure 2), we concentrate on 31.4 GHz (nearly unaffected by snow), 90 GHz (with snow scattering becoming important), and 150 GHz (strongest signal from snow). Figure 5 depicts the measured TBs (small symbols) at the original 1 s time resolution. As expected, the TB dynamic range is spectrally dependent: at 150 GHz, the measured TBs vary between 23 and 69 K; at 90 GHz, the measured TBs vary between 15 and 42 K; whereas at 31.4 GHz, the TB variability ranges from 8 to

16 K. When looking at the dependence of the TB magnitude on SWP derived from the 35 GHz cloud radar measurements (color coded), the clustering in the TB space is consistent with the expectation that larger SWP generally produce higher TBs at 90 and 150 GHz. This clear correlation between SWP and the TB enhancement at 150 GHz (and to some less extent also at 90 GHz) gives evidence that the signals contain a significant contribution from snow scattering.

[43] The crucial scientific question to be answered at this point is, whether the high-frequency TB enhancement caused by a certain snow amount can be disentangled by other radiometric effects, namely, the presence of super-cooled droplets and the specific snow size and habit occurrence. To address this issue we perform a variety of RT simulations.

### 5.2.1. Spectral TB Signatures of Supercooled Cloud Droplets

[44] Because the MWR data do not contain sufficient information about the vertical liquid water profile [Crewell *et al.*, 2009], we have to estimate the uncertainty arising from vertically distributing the HATPRO-derived LWP of up to  $0.1 \text{ kg m}^{-2}$  (Figure 1). Hence, we distributed the LWP in three different ways: (1) in the lowest model layer (100 m above ground), (2) homogeneously distributed over the total cloud depth, and (3) concentrated at the cloud top. The cloud tops detected by the cloud radar within the selected time period vary between 4500 and 5500 m above ground level with temperatures ranging from  $-41^\circ\text{C}$  to  $-46^\circ\text{C}$ . That means a temperature difference for the model liquid water between scenario (1) and (3) of 30–38 K. Scenario (3) is surely an extreme assumption because aircraft observations [e.g., Boudala *et al.*, 2004] reveal that almost all liquid water is found at temperatures warmer than  $-40^\circ\text{C}$ . Hence, scenario (3) can be seen more as a lower boundary assumption for the possible liquid water temperature.

[45] In Figure 5 (first and third frames), the TBs simulated for the three LWP configurations are shown together with the corresponding observations for 150, 90, and 31.4 GHz. Although the simulated values are averaged on a 10 min time interval, the measured TBs are shown in the original 1 s time resolution to illustrate the high temporal variability in the measurements. The simulations reveal that the signal emitted by liquid water is mainly a function of mass and temperature. The largest impact of liquid water positioning is found at higher frequencies: For the highest LWP value of  $0.1 \text{ kg m}^{-2}$ , the TB differences reach 15 (6) K at 150 (90) GHz, whereas at 31.4 GHz, the differences are below 1 K. Both at 150 and 90 GHz, the TBs generally increase with the temperature of the liquid water layer (i.e., the highest 150 GHz TBs occur for the liquid water in the lowest layer). The low impact at 31.4 GHz is important because otherwise LWP estimates (based on 22–31 GHz channels) would not be trustworthy.

[46] If compared to measurements, the simulated TBs agree rather well for both frequency combinations 150/31.4 GHz and 90/31.4 GHz (Figure 5). Unfortunately, the uncertainty induced by the unknown liquid water temperatures is so large that the whole range of observations can be explained by variable liquid water positioning. To narrow down the possible range, we look again at the cloud radar observations (Figure 1, second frame). In the Doppler velocity profile one can detect a band of enhanced fall velocities between 500 and 2000 m. Changes in fall velocity are often connected to a change in particle habits and riming processes. These observations give indication that the scenario of all liquid water being concentrated close to ground is not very likely. If this scenario is excluded, there remains a “branch” of measurements in which enhanced 150 GHz TBs cannot be explained by liquid water alone and are likely to be caused by scattering at snow particles (Figure 5). This is supported by the fact that this branch corresponds to those times when the cloud radar observed the strongest SWP of  $>0.15 \text{ kg m}^{-2}$ .

### 5.2.2. Spectral TB Signatures of Snow

[47] The RT simulations are repeated adding the snow water content profile for different snow habits and SSD parameters. Ten minute averaged SWC profiles are determined using the temperature-dependent Z-SWC relation

given by Hogan *et al.* [2006]. The simulations are performed for the three different snow types 6bR, SEC, and DEN and a constant  $N_0$  of  $1 \times 10^7 \text{ m}^{-4}$ . Liquid water is assumed to be distributed homogeneously in the vertical as an average of the two extreme scenarios: cloud top and base.

[48] The additional contribution of snow causes the TBs to increase especially at the higher frequencies (Figure 5, second and fourth frames). Again, snow shape strongly influences the total scattering signal: Similarly, to the former discussion, the maximum TB enhancement is caused by 6bR followed by SEC and DEN. At 150 GHz, the measurements seem to be covered best by DEN, whereas at 90 GHz, their scattering signals seem to be too small. However, as mentioned before, it is necessary to know the true vertical profiles of liquid water,  $N_0$ , and shape to fully explain the real TB patterns.

[49] To get a better view of the signal caused by snow, we can use the RT model results to calculate the TB differences between the pure liquid and the liquid water plus snow case. Again, calculations are performed for the three different habits and the two  $N_0$  values (Figure 6). In general, the TB differences (dTB) and the snow scattering signal increase with SWP and frequency. For all frequencies and shapes, the differences are higher for lower  $N_0$  values, i.e., SSDs containing larger particles. Considering the higher  $N_0$  of  $1 \times 10^7 \text{ m}^{-4}$  (i.e., the narrower SSD), the dTB at 150 GHz vary for the largest SWP of  $0.23 \text{ kg m}^{-2}$  between 7 and 18 K depending on particle shape. At 90 GHz, the snow signal is lower by a factor of 4.5 and ranges at maximum between 1.5 and 4 K. The snow signal at 31.4 GHz of 0.1–0.2 K is lower than the instrument noise and therefore negligible. To compare the scattering effect to those of satellite sensors, RT calculations were also performed for nadir geometry (not shown). The analogous TB depression for the satellite sensor is 50% (40%) lower at 150 (90) GHz compared to the simulated TB enhancement for the ground-based sensor. Sensitivities to snow shape and  $N_0$  are similar for both geometries, although the uncertainty caused by the unknown surface albedo is much weaker for the ground-based measurements.

[50] If  $N_0$  is reduced by a factor of 10 (i.e., broader SSD containing large particles), the dTB are enhanced: At 150 GHz and high SWP values the dTB range from 15 to 38 K depending on snow habit. This is higher by a factor of 2 compared to the more narrow SSD. At 90 GHz, the dTB increase by a slightly higher factor of 2.5 and range between 4 and 10 K, whereas at 31.4 GHz, the signal is still low with values between 0.2 and 0.5 K. Interestingly, the TB increase toward lower  $N_0$  differs for the three particle types: While at higher  $N_0$  the differences between 6bR and SEC are low, they increase strongly at lower  $N_0$  both at 150 and 90 GHz. On the other hand, DEN differs significantly from 6bR and SEC for both  $N_0$  values. To explain this behavior, we have to consider both the single scattering properties of the different particle types and the SSDs. Both are affected by  $N_0$  and the chosen particle shape over the mass size relation (equation (3)). Considering the particle's single scattering properties (Figure 3), the scattering efficiencies for SEC and 6bR are quite similar up to a size parameter of 1.5. In contrast, scattering efficiencies for DEN begin to deviate significantly from 6bR and SEC at a much lower size parameter of 0.8. Additionally, the mass

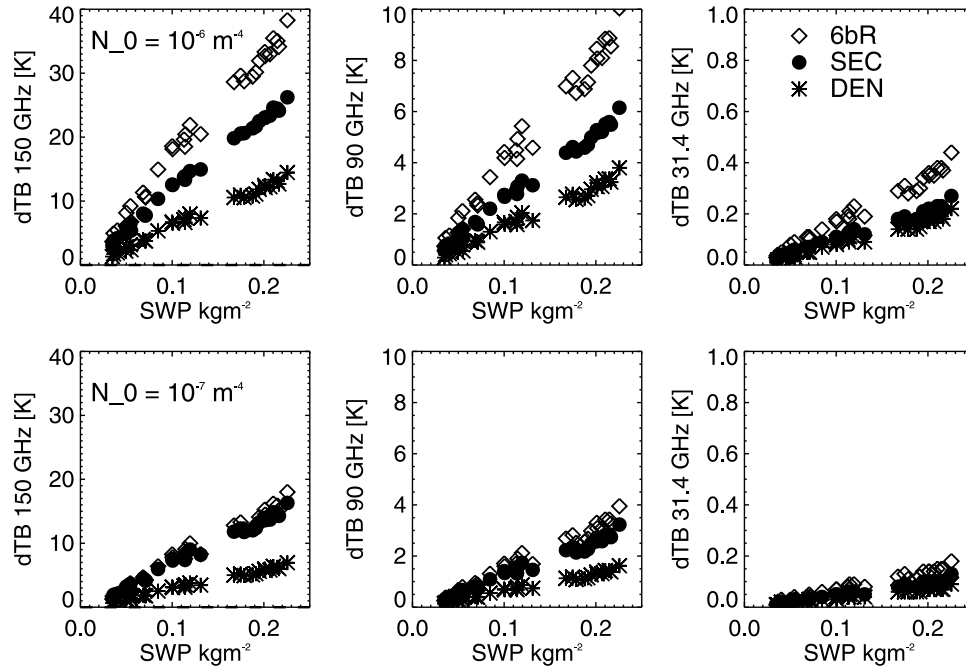


**Figure 6.** TB-differences (dTb) for (left) 150 GHz, (middle) 90 GHz, and (right) 31.4 GHz based on the data shown in Figure 5 between the simulations for only homogeneously distributed liquid water and liquid water combined with snow (SWP in  $\text{kg m}^{-2}$  at the abscissas). (top) dTB for  $N_0 = 1 \times 10^6 \text{ m}^{-4}$  (broad SSD) and (bottom)  $N_0 = 1 \times 10^7 \text{ m}^{-4}$  (narrow SSD). The different symbols correspond to different snow shapes: 6bR (diamonds), SEC (circles), and DEN (asterisks).

size relation for DEN influences the slope of the SSD. DEN have to be considerably larger to have an equal mass compared to, e.g., 6bR. Thus, the SSD of DEN will always be broader compared to a SSD with “denser” particle shapes and the same  $N_0$ .

[51] Figure 6 also illustrates the errors because of the wrong SSD or snow shape that would arise in a simple one-channel retrieval with perfect knowledge of the atmospheric environment (humidity, temperature, and liquid water profile). For example, setting the snow type to DEN and  $N_0$  to  $1 \times 10^6 \text{ m}^{-4}$ , a dTB of 15 K at 150 GHz results in a SWP of  $0.22 \text{ kg m}^{-2}$ . Assuming the similar particle type, SEC would provide an SWP estimate of only  $0.12 \text{ kg m}^{-2}$  and thus an error of 50%. A similar comparison can be done by keeping the particle shape constant (e.g., SEC) and changing  $N_0$  from  $1 \times 10^6$  to  $1 \times 10^7 \text{ m}^{-4}$ , again assuming a dTB of 15 K. The retrieved SWP changes from 0.12 to  $0.22 \text{ kg m}^{-2}$  because of the change of the SSD by 1 order of magnitude. In summary, this sensitivity study reveals that both SSD parameters  $N_0$  and snow shape are key quantities for any snow retrieval development based on MW observations.

## 6. Toward Algorithm Development

[52] Our ultimate goal is the development of an optimal retrieval algorithm for snow characteristics from different possible suites of instruments. As a first step, it is paramount to understand the different spectral properties (absorption, scattering, backscattering) of the atmospheric variables to be retrieved. As we could see in the former case study, not only the total snow mass but also SSD parameters like  $N_0$  and snow shape strongly affect the scattering signal. To inves-

tigate these dependencies in more detail and to identify possible synergy benefits of active and passive microwave instruments, we look at RT simulations for different combinations of SWP,  $N_0$ , and shape and analyze their signatures in the TB and reflectivity space. The simulations are performed for a constant atmosphere (on 8 February 2009, at 08:20 UTC) and a 5 km thick single layer cloud containing only homogeneously distributed snow (SWP ranging from 0.1 to  $0.4 \text{ kg m}^{-2}$ ) without any other hydrometeors present. To compare TB signals, which always provide a vertically integrated information, with range-resolved reflectivities, we integrate the radar reflectivities over height (nonlogarithmic).

[53] Figure 7 (first row) shows an almost linear TB increase with SWP at 90 and 150 GHz. Again (see section 4), the scattering signature by 6bR causes the TB to increase the strongest followed by SEC and DEN, whereas higher  $N_0$  values significantly reduce the signal (right versus left column). The deviations of the different shapes are more pronounced for higher SWP and lower  $N_0$  values. For example, at  $N_0 = 1 \times 10^6 \text{ m}^{-4}$ , the shape uncertainty can cause an error in SWP by a factor of 2. The reason for this effect is again that higher SWP and/or lower  $N_0$  values broaden the SSD. In consequence, larger particles with significant shape-dependent single scattering properties begin to dominate the signal. In the TB space a large overlap of the different shape and SWP combinations is evident. This means that changing SWP or shape in the given range has no significant different effects in the TB space for 90 and 150 GHz. Thus, the retrieval of SWP from the 150/90 GHz TB signal alone is only reasonable with an assumption about shape and  $N_0$ , which are usually unknown.

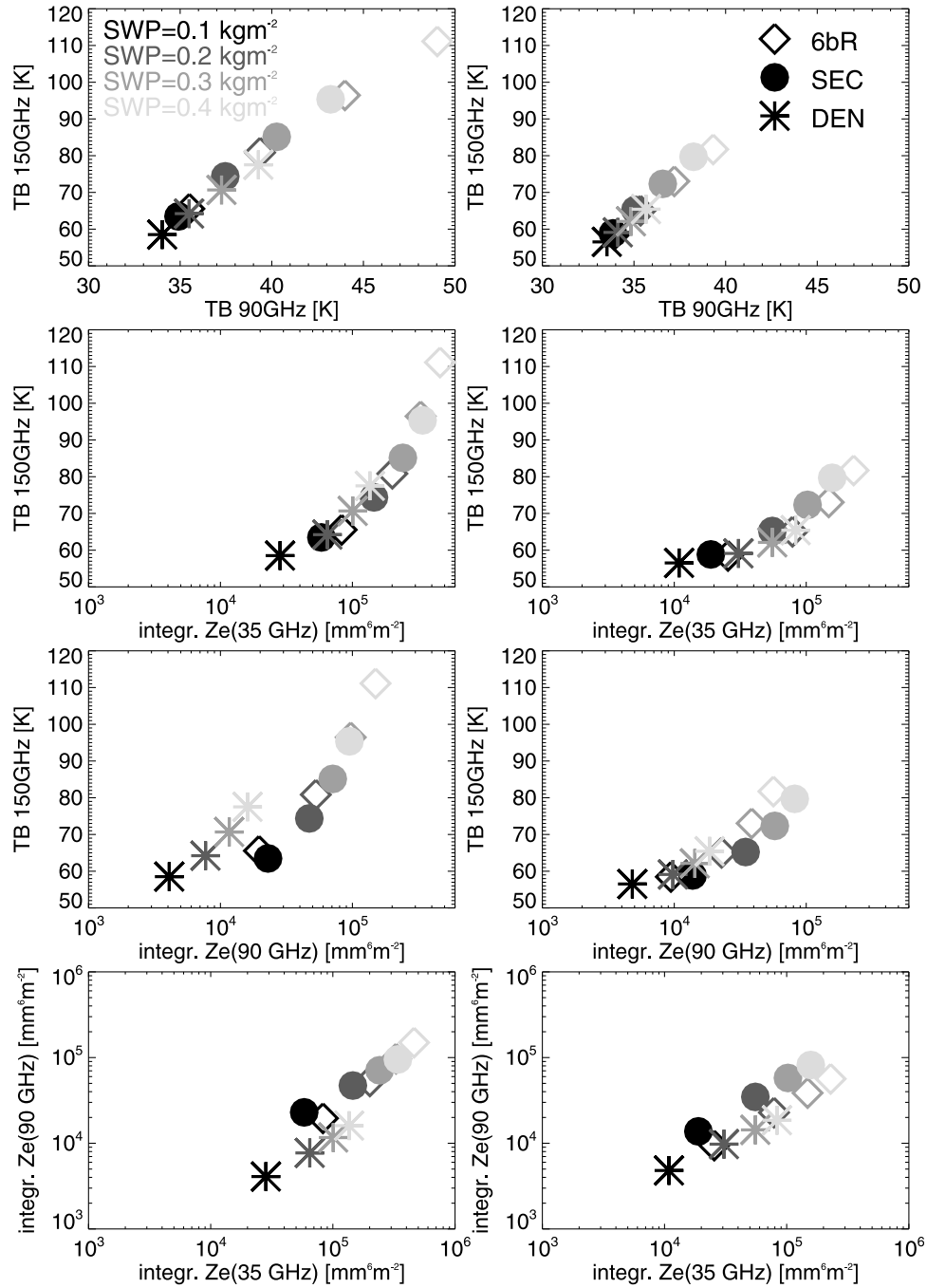


**Figure 7.** Simulated passive TB in K and vertically integrated radar reflectivity in  $\text{mm}^6 \text{ m}^{-2}$  factor for a constant atmosphere and different snow microphysics: model results (left) for  $N_0 = 1 \times 10^6 \text{ m}^{-4}$  and (right) for  $N_0 = 1 \times 10^7 \text{ m}^{-4}$ . The symbols represent different snow habits similar to Figures 5 and 6: 6bR (diamonds), SEC (circles), and DEN (asterisks), whereas the different gray scale illustrates different SWP values ranging from 0.1 to 0.4  $\text{kgm}^{-2}$ . First row: TB at 150 and 90 GHz, second row: TB 150 GHz and integrated Ze at 35 GHz, third row: TB 150 GHz and integrated Ze at 90 GHz, and fourth row: integrated Ze at 90 GHz and 35 GHz.

[54] If the TBs at 150 GHz are combined with integrated radar reflectivities at 35 GHz (second row in Figure 7), the overlap between different habits is still present. Again, the assumptions about shape and  $N_0$  are crucial for retrieving SWP. The errors can still be up to a factor of 2 if, for example, one assumes DEN instead of SEC. Using a higher radar frequency of 90 GHz combined with the 150 GHz

scattering signal (Figure 7, third row), however, allows a first shape separation, especially between DEN and the other two shapes (6bR and SEC) for  $N_0 = 1 \times 10^6 \text{ m}^{-4}$ . This can be explained by the increasing shape sensitivity in the backscattering with increasing size parameter or frequency, respectively. Combining only radar information at 35 and

90 GHz (Figure 7, lowest frame) allows some shape separation, especially for the lowest  $N_0$  values.

[55] In summary, we can conclude from this sensitivity study that the combination of passive and active remote sensing could be rather useful for the development of snow retrieval algorithms to account for the large uncertainties due to shape and SSD variability. An interesting aspect shown by *Westbrook et al.* [2004] is that the aggregation process, which is the dominant mechanism for the formation of large snowflakes, shows some kind of universality. For example, both in situ measurements and model studies have shown that the fractal dimension of snowflakes, which is related to the parameter  $b$  in the mass size relation (equation (1)), is around 2. If such universal behavior of the SSD can be related to single scattering properties, this would exceedingly simplify the retrieval development.

## 7. Conclusions

[56] In this study we investigated the sensitivity of ground-based passive MWR measurements in the frequency range 22–150 GHz to snowfall characteristics. Several remote sensing and in situ observations from 8 February 2009 were used to reconstruct the atmospheric state for a 5 h time period. On the basis of this data set, we performed several RT simulations, which enabled us to analyze the influence of liquid water profile, snow shape, SSD, and SWP on the ground-based TB.

[57] On the basis of the results of this study, we can draw the following conclusions:

[58] 1. The proposed snow scattering effect of a TB enhancement in ground-based measurements could be identified at 90 and 150 GHz with the help of a 35 GHz cloud radar. During a 5 h snow event, the radar-derived SWP values (up to  $0.2 \text{ kg m}^{-2}$ ) lead to an TB enhancement of about 8 K at 150 GHz and 4 K at 90 GHz, whereas at 31.4 GHz, the signal change was below 1 K.

[59] 2. Significant amounts of liquid water (LWP up to  $100 \text{ gm}^{-2}$ ) were detected during the investigated snowfall event. Their vertical distribution and thus their temperature-dependent emission were simulated for extreme cloud positions. It revealed that the uncertainty in the liquid water profile is able to totally obscure the snow scattering signal. Nonnegligible amounts of supercooled liquid water were also found in several aircraft studies and thus appear to be normal and not an exception. Hence, the accurate modeling of the radiative properties of supercooled water is essential for every snow retrieval algorithm using microwave frequencies for both ground-based and satellite observations.

[60] 3. The observed TB enhancement can be reproduced by simulations using idealized snow crystals with realistic assumptions on SWC and SSD taken from radar and disdrometer measurements. In the given parameter range, the snow scattering signal depends in similar order on varying SWP, shape, and  $N_0$ . Hence, the question, if the scattering properties of the idealized crystals are representative for natural snow, could not be answered, considering the uncertainty in SSD and SWC.

[61] 4. The optical disdrometer measurements reveal that for our case study a snow fraction of 1%–2% has sizes larger than 10 mm, whereas the radar-derived snow water path was lower than  $0.2 \text{ kg m}^{-2}$ . Therefore, radiative transfer calcu-

lations especially for radar applications should account for particles larger than 10 mm, and scattering databases for those large aggregates are needed. Area ratio was considered as one possible parameter to characterize snow shape; however, the idealized particles show too low values compared to the disdrometer measurements, especially when the particle size increases.

[62] 5. RT simulations with different combinations of snow shape,  $N_0$ , and SWP values showed that the ground-based passive MW signals up to 150 GHz are not solely able to distinguish between those three parameters. Similar to earlier studies that investigated the downward measuring perspective, we found for the upward looking geometry that the combination of active and passive MW instruments allows a significantly better separation of the different microphysical snow parameters.

[63] 6. For our case, the amplitude of the TB enhancement observed by a ground-based sensor is by a factor of  $\sim 2$  higher than that of the TB depression measured by a nadir viewing sensor while showing similar sensitivities to SSD and particle shape. In addition, ground-based observations are less affected by the unknown surface albedo. Further, the good infrastructure with possibilities to set up further instruments makes ground-based observations ideally suited to support current and future satellite retrieval development.

[64] In the future we will expand our investigation to the whole TOSCA data set with special emphasis, e.g., on the frequency and amount of liquid water in snowing conditions and their dependence on other parameters like snow intensity or ground temperature. We will further statistically analyze snow microphysical characteristics like shape and SSD and moreover investigate their influence on the passive and active MW observations. Simultaneously, passive measurements at frequencies higher than 150 GHz combined with radar systems above 35 GHz should be investigated to test their potential for snow measurements.

## Appendix A: Comparison of Idealized Snow Habits With 2DVD Measurements

[65] Information on single scattering characteristics are often limited to a certain size range and currently only available for idealized snow habits. In this section we analyze (1) how many particles are exceeding a certain size limit and (2) how realistic are the model crystals compared to 2DVD measurements by considering the particles' area and aspect ratios. The analyses are made for the time period 07:30–12:40 UTC according to the model comparison. Considering smaller time periods did not significantly change the results.

### A1. Snow Size

[66] Because the radiative properties of large particles ( $>10 \text{ mm}$ ) are widely unknown, we analyze the natural upper snow size limit and the frequency of large sized SSD for our case study. Analyzing the relative fraction of large snow particles gives us indirect information about their importance for radiative transfer. On the basis of the 2DVD measurements, we calculate the cumulative probability function (CPF) and investigate their dependence on the radar derived SWP (Figure A1). The CPFs reveal that only 1%–2% of the

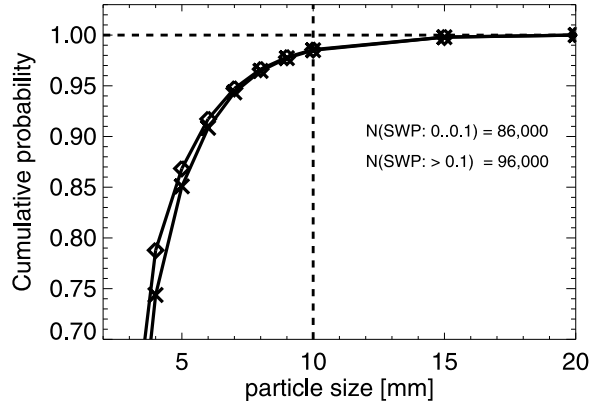


**Figure A1.** Cumulative probability functions (CPF) for snow particle sizes measured with the 2DVD from the time period 8 February 2009, 07:30–12:40 UTC. The CPF is divided into two SWP groups (derived from cloud radar measurements): 0–0.1 kg m<sup>-2</sup> (diamonds) and >0.1 kg m<sup>-2</sup> (crosses).

particles are larger than 10 mm (i.e., the upper database size limit). Although the amount of detected large particles is relatively small, these particles could have a significant impact on radar applications because of their backscattering dependence on the sixth moment of the particle diameter. The CPFs for different SWP ranges are similar with slightly more small particles in the SWP range below 0.1 kg m<sup>-2</sup>. This is consistent to the small variations of the formerly derived parameters  $N_0$  and  $\lambda$  for the assumed exponential SSDs in Figure 1, fourth frame (07:30–12:40 UTC).

## A2. Snow Shape Comparison

[67] As mentioned before, it is quite challenging to find an appropriate parameter for snow shape. The fractal dimension  $d_f$  is often used to characterize fractal structures like aggregates [e.g., Westbrook *et al.*, 2004; Ishimoto, 2008]. To derive  $d_f$  for snow it would be necessary to capture the whole 3-D structure of the particle, which is not fully possible with the 2DVD's two 2-D projections. The study by Korolev and Isaac [2003] investigated shape properties of ice particles measured by an airborne optical probe. Similar to their work, we derived the area ratio  $A_{rr}$  and the aspect ratio  $A_{sr}$  of the measured particles, which are defined as

$$A_{rr} = \frac{4A}{\pi D^2} \quad (\text{A1})$$

$$A_{sr} = \frac{D_{\min}}{D} \quad (\text{A2})$$

with  $A$  as the particles projected area and  $D$  ( $D_{\min}$ ) the maximum (minimum) particle diameter of the circumscribed ellipse.  $A_{rr}$ , defined as the ratio of the particle projected area to the area of the circumscribed circle with radius  $D/2$ , can be interpreted as roundness or area density. If the projected particle is perfectly “round,”  $A_{rr}$  is 1, while the values decrease when the area becomes small compared to the maximum size  $D$ . The second shape parameter is the aspect ratio  $A_{sr}$ , which is defined here as the ratio of the minimum to the maximum diameter of the circumscribed ellipse.

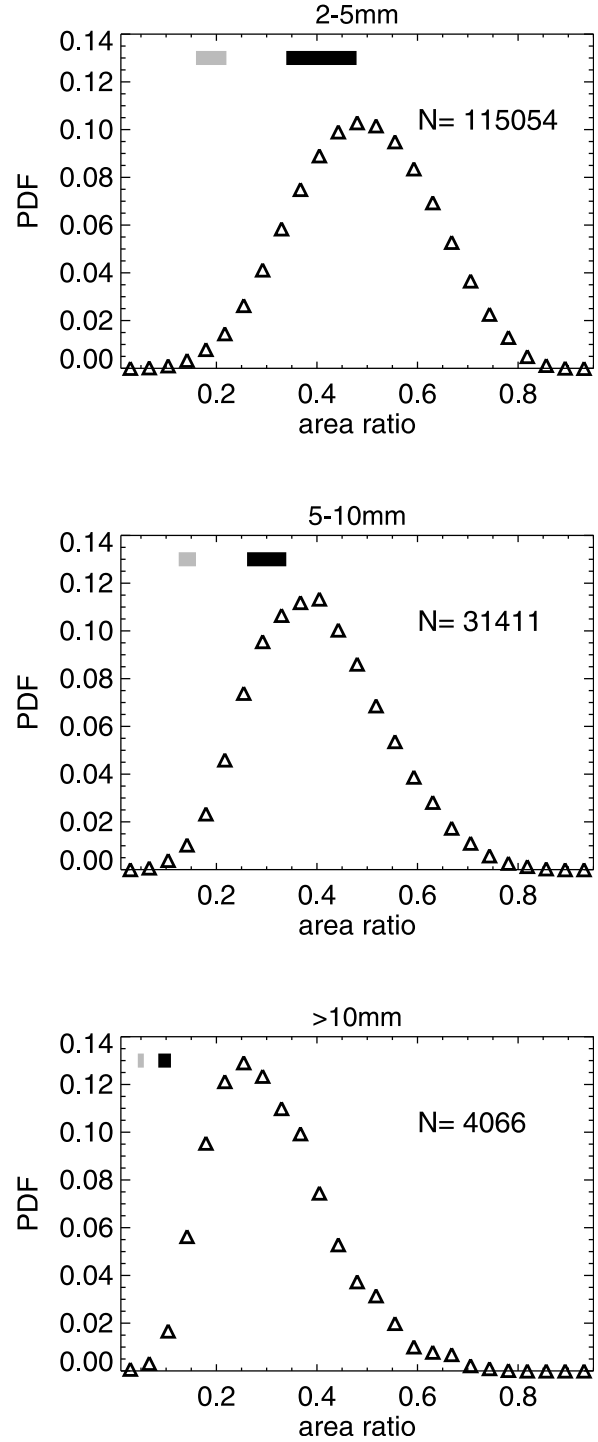


**Figure A2.** Probability density functions (PDFs) of area ratios (particle projected area divided by the area of the smallest circumscribed circle; for more details see text) for different maximum particle size ranges: (top) 2–5 mm, (middle) 5–10 mm, and (bottom) >10 mm. The data are from the 8 February 2009 and the time period 07:30–12:40 UTC. The thick solid lines indicate the area ratio range for the given  $D$  range and idealized crystals: SEC/DEN (black) and 6bR (gray).



[68] The probability density functions of  $A_{\text{rr}}$  and  $A_{\text{sr}}$  are calculated for different size ranges: 2–5 mm, 5–10 mm, and >10 mm. As mentioned by *Korolev and Isaac* [2003], the main error source for determining  $A_{\text{rr}}$  and  $A_{\text{sr}}$ , when neglecting errors caused by the optical system, is the ratio between particle size and pixel resolution. To minimize those errors, we consider only particles larger than 2 mm (i.e., 10 pixels according to the 2DVD resolution of 0.2 mm). The derived aspect ratios  $A_{\text{sr}}$  (not shown) remain nearly constant at 0.6 in every size class. In contrast, the maximum of the  $A_{\text{rr}}$  distribution (Figure A2) continuously decreases from 0.5 to 0.25 as snow size increases. Even though the maximum particle size investigated by *Korolev and Isaac* [2003] was limited to 1 mm, their results principally agree with the 2DVD measurements: They found for their largest particles and temperature range of  $-10^{\circ}\text{C}$  to  $-15^{\circ}\text{C}$   $A_{\text{sr}}$  around 0.6, not significantly dependent on size. Similar to our results, they show a decreasing  $A_{\text{rr}}$  toward larger sizes. The  $A_{\text{rr}}$  value for their largest particle size of 1 mm, however, is with 0.4 slightly lower compared to our results of 0.5 in the lowest size class of 2–5 mm.

[69] In the following we compare the shape characteristics from the 2DVD measurements with idealized particles used for the RT simulations. The aspect ratio for the totally symmetric 6bR is always between 0.7 and 1. For SEC and DEN, the  $A_{\text{sr}}$  ranges from almost zero to 1 depending on their orientation. We therefore concentrate on area ratio parameter  $A_{\text{rr}}$ . The idealized particle's  $A_{\text{rr}}$  values can be calculated according to the relations given by *Liu* [2004] and *Noh et al.* [2006]

$$A_{\text{rr}} = 0.261d_{\text{max}}^{-0.377} \quad (\text{A3})$$

$$A_{\text{rr}} = 0.125d_{\text{max}}^{-0.351} \quad (\text{A4})$$

with the maximum particle dimension  $d_{\text{max}}$  in centimeter. Equation (A3) is applicable for both SEC and DEN, whereas equation (A4) is valid for 6bR. Equations (A3) and (A4) were applied to the different size regimes in Figure A2. Again, assuming the idealized snow particles fall randomly oriented, these values represent an upper limit of the real  $A_{\text{rr}}$ . In the different size ranges, the  $A_{\text{rr}}$  values for 6bR are always below the maximum of the measured distribution. While DEN and SEC reach the measured maximum in the lowest size regime from 0.4 to 2 mm, they have lower  $A_{\text{rr}}$  values, if snow size increases. Also, the spread of the idealized particle's  $A_{\text{rr}}$  values decreases strongly if moving to larger particles. Summarized, this simple shape comparison again gives evidence that the considered model particles are less realistic, if going to larger particle sizes. This indirectly confirms the results of several observations that aggregate structures dominate the large end of SSDs.

[70] **Acknowledgments.** This work is part of the TOSCA project funded by the German Science Foundation (DFG) under grant LO 901/3-1. We thank the UFS team under the lead of Markus Neumann for their support with the deployment and maintenance of all instruments. We are indebted to Schönhuber and Lammer from Joanneum Research (Graz, Austria) for their great support and for providing the 2DVD. We also greatly acknowledge Martin Hagen (German Aerospace Center), Gerhard Peters (Max-Planck Institute for Meteorology, Hamburg), and Matthias Wiegner (University of Munich) for providing their instrumentation within the TOSCA campaign. Further, the authors thank Lutz Hirsch (MPI Hamburg) and Stephanie Redl (University of Cologne) for their great work in data

processing. The comments and suggestions from four anonymous reviewers are also gratefully acknowledged.

## References

- Bennartz, R., and G. W. Petty (2001), The sensitivity of microwave remote sensing observations of precipitation to ice particle size distributions, *J. Appl. Meteorol.*, **40**, 345–364, doi:10.1175/1520-0450(2001)040<0345:TSOMRS>2.0.CO;2.
- Bennartz, R., and P. Bauer (2003), Sensitivity of microwave radiances at 85–183 GHz to precipitating ice particles, *Radio Sci.*, **38**(4), 8075, doi:10.1029/2002RS002626.
- Bertolini, D., M. Cassettari, and G. Salvetti (1982), The dielectric relaxation time of supercooled water, *J. Chem. Phys.*, **76**, 3285–3290.
- Boudala, F. S., G. A. Isaac, S. G. Cober, and Q. Fu (2004), Liquid fraction in stratiform mixed-phase clouds from in situ observations, *Q. J. R. Meteorol. Soc.*, **130**, 2919–2931.
- Brandes, E. A., K. Ikeda, G. Zhand, M. Schönhuber, and R. M. Rasmussen (2007), A statistical and physical description of hydrometeor distributions in Colorado snowstorms using a Video Disdrometer, *J. Appl. Meteorol. Climatol.*, **46**, 634–650, doi:10.1175/JAMC2489.1.
- Crewell, S., K. Ebell, U. Löhnert, and D. D. Turner (2009), Can liquid water profiles be retrieved from passive microwave zenith observations?, *Geophys. Res. Lett.*, **36**, L06803, doi:10.1029/2008GL036934.
- Ellis, T. D., T. L'Ecuyer, J. M. Haynes, and G. L. Stephens (2009), How often does it rain over the global oceans? The perspective from CloudSat, *Geophys. Res. Lett.*, **36**, L03815, doi:10.1029/2008GL036728.
- Ellison, W. (2006), Freshwater and sea water, in *Thermal Microwave Radiation—Applications for Remote Sensing, Ser. IET Electromagnetic Waves Series*, vol. 52, edited by C. Mätzler et al., pp. 431–455, Inst. Eng. Technol., London, U.K.
- Evans, K. F., and G. L. Stephens (1991), A new polarized atmospheric radiative transfer model, *J. Quant. Spectrosc. Radiat. Transfer*, **46**, 413–423.
- Evans, K. F., J. R. Wang, P. E. Racette, G. Heymsfield, and L. Li (2005), Ice cloud retrievals and analysis with the compact scanning submillimeter imaging radiometer and the cloud radar system during CRYSTAL FACE, *J. Appl. Meteorol.*, **44**, 839–859.
- Field, P. R., R. J. Hogan, P. R. A. Brown, A. J. Illingworth, T. W. Choullarton, and R. J. Cotton (2005), Parametrization of ice particle size distributions for mid-latitude stratiform cloud, *Q. J. R. Meteorol. Soc.*, **131**, 1997–2017.
- Grecu, M., and W. S. Olson (2008), Precipitating snow retrievals from combined airborne cloud radar and millimeter-wave radiometer observations, *J. Appl. Meteorol. Climatol.*, **47**, 1634–1650, doi:10.1175/2007JAMC1728.1.
- Han, Y., and E. R. Westwater (2000), Analysis and improvement of tipping calibration for ground-based microwave radiometers, *IEEE Trans. Geosci. Remote Sens.*, **38**, 43–52.
- Hanesch, M. (1999), Fall velocity and shape of snowflakes, Ph.D. thesis, pp. 15–22, Swiss Federal Institute of Technology Zürich.
- Hewison, T. J., and S. J. English (1999), Airborne retrievals of snow and ice surface emissivity at millimeter wavelengths, *IEEE Trans. Geosci. Remote Sens.*, **37**, 1871–1879.
- Heymsfield, A. J., A. Bansemer, P. R. Field, S. L. Durden, J. L. Stith, J. E. Dye, W. Hall, and C. A. Grainger (2002), Observations and parameterizations of particle size distributions in deep tropical cirrus and stratiform precipitating clouds: Results from in situ observations in TRMM field campaigns, *J. Atmos. Sci.*, **59**(24), 3457–3491, doi:10.1175/1520-0469(2002)059<3457:OAPOPS>2.0.CO;2.
- Heymsfield, A. J., P. Field, and A. Bansemer (2008), Exponential size distribution for snow, *J. Atmos. Sci.*, **65**, 4017–4031, doi:10.1175/2008JAS2583.1.
- Hogan, R. J., M. P. Mittermaier, and A. J. Illingworth (2006), The retrieval of ice water content from radar reflectivity factor and temperature and its use in the evaluation of a mesoscale model, *J. Appl. Meteorol. Climatol.*, **45**, 301–317.
- Hong, G. (2007), Parameterization of scattering and absorption properties of nonspherical ice crystals at microwave frequencies, *J. Geophys. Res.*, **112**, D11208, doi:10.1029/2006JD008364.
- Huang, G.-J., V. N. Bringi, R. Cifelli, D. Hudak, and W. A. Petersen (2009), A methodology to derive radar reflectivity–liquid equivalent snow rate relations using C-Band radar and a 2-D video disdrometer, *J. Atmos. Oceanic Technol.*, accepted.
- Ishimoto, H. (2008), Radar backscattering computations for fractal-shaped snowflakes, *J. Meteorol. Soc. Jpn.*, **86**, 459–469.
- Katsumata, M., H. Uyeda, K. Iwanami, and G. Liu (2000), The response of 36- and 89-GHz microwave channels to convective snow clouds over ocean: Observation and modeling, *J. Appl. Meteorol.*, **39**, 2322–2335.

- Kim, M.-J. (2006), Single scattering parameters of randomly oriented snow particles at microwave frequencies, *J. Geophys. Res.*, **111**, D14201, doi:10.1029/2005JD006892.
- Korolev, A., and G. Isaac (2003), Roundness and aspect ratio of particles in ice clouds, *J. Atmos. Sci.*, **60**(15), 1795–1808.
- Kruger, A., and W. F. Krajewski (2002), Two-Dimensional video disdrometer: A description, *J. Atmos. Ocean. Technol.*, **19**(5), 602–617.
- Kulie, M. S., and R. Bennartz (2009), Utilizing space-borne radars to retrieve dry snowfall, *J. Appl. Meteorol. Climatol.*, **48**, 2564–2580, doi:10.1175/2009JAMC2193.1.
- Kusunoki, K., M. Murakami, N. Orikasa, M. Hoshimoto, Y. Tanaka, Y. Yamada, H. Mizuno, K. Hamazu, and H. Watanabe (2005), Observation of quasi-stationary and shallow orographic snow clouds: Spatial distributions of supercooled liquid water and snow particles, *Mon. Weather Rev.*, **133**, 743–751, doi:10.1175/MWR2874.1.
- Liebe, H. J., G. A. Hufford, and T. Manabe (1991), A model for the permittivity of water at frequencies below 1THz, *Internat. J. Infrared Mill. Waves*, **12**, 659–675.
- Liljegren, J. C., S. A. Boukabara, K. Cady-Pereira, and S. A. Clough (2005), The effect of the half-width of the 22-GHz water vapor line on retrievals of temperature and water vapor profiles with a 12-channel microwave radiometer, *IEEE Trans. Geosci. Remote Sens.*, **43**, 1102–1108.
- Liu, G. (2004), Approximation of single scattering properties of ice and snow particles for high microwave frequencies, *J. Atmos. Sci.*, **61**, 2441–2456.
- Liu, G. (2008a), Deriving snow cloud characteristics from CloudSat observations, *J. Geophys. Res.*, **113**, D00A09, doi:10.1029/2007JD009766.
- Liu, G. (2008b), A database of microwave single-scattering properties for nonspherical ice particles, *Bull. Amer. Meteor. Soc.*, **89**, 1563–1570, doi:10.1175/2008BAMS2486.1.
- Löhnert, U., S. Crewell, A. Macke, and C. Simmer (2001), Profiling cloud liquid water by combining active and passive microwave measurements with cloud model statistics, *J. Atmos. Ocean. Technol.*, **18**, 1354–1366.
- Lynn, B. H., A. P. Khain, J. Dudhia, D. Rosenfeld, A. Pokrovsky, and A. Seifert (2005), Spectral (Bin) microphysics coupled with a mesoscale model (MMS). Part I: Model description and first results, *Mon. Weather Rev.*, **133**, 44–58, doi:10.1175/MWR-2840.1.
- Matrosov, S. Y. (2007), Modeling backscatter properties of snowfall at millimeter wavelength, *J. Atmos. Sci.*, **64**, 1727–1736, doi:10.1175/JAS3904.1.
- Melchionna, S., M. Bauer, and G. Peters (2008), A new algorithm for the extraction of cloud parameters using multipeak analysis of cloud radar data—First application and preliminary results, *Meteor. Zeitschrift*, **17**, 613–620.
- Muramoto, K.-I., K. Matsuura, and T. Shiina (1995), Measuring the density of snow particles and snowfall rate, *Electron. Comm. Jpn.*, **3**, 78, 71–79, doi:10.1002/ecjc.4430781107.
- Nešpor, V., W. F. Krajewski, and A. Kruger (2000), Wind-induced error of raindrop size distribution measurement using a two-dimensional video disdrometer, *J. Atmos. Oceanic Technol.*, **17**, 1483–1492.
- Noh, Y.-J., G. Liu, E.-K. Seo, J. R. Wang, and K. Aonashi (2006), Development of a snowfall retrieval algorithm at high microwave frequencies, *J. Geophys. Res.*, **111**, D22216, doi:10.1029/2005JD006826.
- Noh, Y.-J., G. Liu, A. S. Jones, and T. H. Vonder Haar (2009), Toward snowfall retrieval over land by combining satellite and in situ measurements, *J. Geophys. Res.*, **114**, D24205, doi:10.1029/2009JD012307.
- Petty, G. W., and W. Huang (2010), Microwave backscatter and extinction by soft ice spheres and complex snow aggregates, *J. Atmos. Sci.*, **67**, 769–787, doi:10.1175/2009JAS3146.1.
- Ray, P. S. (1972), Broad-band complex refractive indexes of ice and water, *Appl. Optics*, **11**, 1836–1844.
- Rose, T., S. Crewell, U. Löhnert, and C. Simmer (2005), A network suitable microwave radiometer for operational monitoring of the cloudy atmosphere, *Atmos. Res.*, **75**, 183–200, doi:10.1016/j.atmosres.2004.12.005.
- Rosenkranz, P. W. (1998), Water vapour microwave continuum absorption: A comparison of measurements and models, *Radio Sci.*, **33**, 919–928, doi:10.1029/98RS01182.
- Seifert, A., and K. Beheng (2006), A two-moment cloud microphysics parameterization for mixed phase clouds. Part 1: Model description, *Meteor. Atmos. Phys.*, **92**, 45–66.
- Seo, E.-K., and G. Liu (2005), Retrievals of cloud ice water path by combining ground cloud radar and satellite high-frequency microwave measurements near the ARM SGP site, *J. Geophys. Res.*, **110**, D14203, doi:10.1029/2004JD005727.
- Smith, P. L., and D. V. Kliche (2005), The bias in moment estimators for parameters of drop size distribution functions: Sampling from exponential distributions, *J. Appl. Meteor.*, **44**, 1195–1205, doi:10.1175/JAM2258.1.
- Skofronick-Jackson, G. M., J. R. Wang, G. M. Heymsfield, R. Hood, W. Manning, R. Meneghini, and J. A. Weinman (2003), Combined radiometer-radar microphysical profile estimations with emphasis on high-frequency brightness temperature observations, *J. Appl. Meteor.*, **42**(4), 476–486.
- Skofronick-Jackson, G. M., M.-J. Kim, J. A. Weinman, and D.-E. Chang (2004), A physical model to determine snowfall over land by microwave radiometry, *IEEE Trans. Geosci. Remote Sens.*, **42**, 1047–1058, doi:10.1109/TGRS.2004.825585.
- Stephens, G. L., et al. (2002), The CLOUDSAT mission and the A-train, *Bull. Am. Meteorol. Soc.*, **83**(12), 1771–1790, doi:10.1175/BAMS-83-12-1771.
- Stogryn, A. P., H. T. Bull, K. Ruay, and S. Iravanchy (1995), *The microwave permittivity of sea and fresh water*, Aerojet Internal Report, Aerojet, Sacramento, Calif.
- Troitsky, A. V., A. M. Osharin, A. V. Korolev, and J. W. Strapp (2003), Polarization of thermal microwave atmospheric radiation due to scattering by ice particles in clouds, *J. Atmos. Sci.*, **60**(13), 1608–1620.
- Turner, D. D., U. Löhnert, M. Cadeddu, S. Crewell, and A. Vogelmann (2009), Modifications to the water vapor continuum in the microwave suggested by ground-based 150 GHz observations, *IEEE Trans. Geosci. Remote Sens.*, **47**, 3326–3337, doi:10.1109/TGRS.2009.202262.
- Waliser, D., et al. (2009), Cloud ice: A climate model challenge with signs and expectations of progress, *J. Geophys. Res.*, **114**, D00A21, doi:10.1029/2008JD010015.
- Westbrook, C. D., R. C. Ball, P. R. Field, and A. J. Heymsfield (2004), Universality in snowflake aggregation, *Geophys. Res. Lett.*, **31**, L15104, doi:10.1029/2004GL020363.
- Yan, B., F. Weng, and H. Meng (2008), Retrieval of snow surface microwave emissivity from the advanced microwave sounding unit, *J. Geophys. Res.*, **113**, D19206, doi:10.1029/2007JD009559.
- Zawadzki, I., F. Fabry, and W. Szyrmer (2001), Observations of supercooled water and secondary ice generation by a vertically pointing X-band Doppler radar, *Atmos. Res.*, **59–60**, 343–359.

A. Battaglia, Earth Observation Science, Earth Observation Centre, Department of Physics and Astronomy, University of Leicester, Leicester, LE1 7RH United Kingdom.

S. Crewell, S. Kneifel, and U. Löhnert, Institute for Geophysics and Meteorology, University of Cologne, Zùlpicherstrasse 49a, 50674 Cologne, Germany. (skneifel@meteo.uni-koeln.de)

D. Siebler, Deutsches Zentrum für Luft- und Raumfahrt, Institut für Physik der Atmosphäre, Oberpfaffenhofen, 82234 WeBling, Germany.